RESEARCH

Transient hygro- and hydro-expansion of freely and restrained dried paper: the fiber-network coupling

Niels H. Vonk[1] · Eline P. C. van Spreuwel[2,3] · Thomas Anijs[3] · Ron H. J. Peerlings[1] · Marc G. D. Geers[1] · Johan P. M. Hoefnagels[1]

Abstract

The transient dimensional changes during *hygro*-expansion and *hydro*-expansion of freely and restrained dried, softwood and hardwood sheets and fibers is monitored, to unravel the governing micro-mechanisms occurring during gradual water saturation. The response of individual fibers is measured using a full-field global digital height correlation method, which has been extended to monitor the transient *hydro*-expansion of fibers from dry to fully saturated. The *hygro*- and *hydro*-expansion is larger for freely versus restrained dried and softwood versus hardwood handsheets. The transient sheet-scale *hydro*-expansion reveals a sudden strain and moisture content step. It is postulated that the driving mechanism is the moisture-induced softening of the so-called "dislocated regions" in the fiber's cellulose micro-fibrils, unlocking further fiber swelling. The strain step is negligible for restrained dried handsheets, which is attributed to the "dislocated cellulose regions" being locked in their stretched configuration during restrained drying, which is supported by the single fiber *hydro*-expansion measurements. Finally, an inter-fiber bond model is exploited and adapted to predict the sheet-scale *hygro*-expansion from the fiber level characteristics. The model correctly predicts the qualitative differences between freely versus restrained dried and softwood versus hardwood handsheets, yet, its simplified geometry does not allow for more quantitative predictions of the sheet-scale *hydro*-expansion.

✉ Johan P. M. Hoefnagels
  j.p.m.hoefnagels@tue.nl

1 Department of Mechanical Engineering, Eindhoven University of Technology, Eindhoven, The Netherlands

2 Department of Physics, Eindhoven University of Technology, Eindhoven, The Netherlands

3 Research & Development, Canon Production Printing, Venlo, The Netherlands

 Springer

Introduction

During inkjet printing, liquid water is supplied on a sheet, resulting in swelling of the paper. In-proper control of swelling and shrinkage can result in unwanted (irregular) out-of-plane deformations, including cockling, fluting, waviness and curl (Kulachenko et al. 2005). To better understand these deformations, and ultimately reduce them, the dimensional stability of paper has been intensively studied. Traditionally, the dimensional stability is studied as *hygro*-expansion (Salmén et al. 1985; Niskanen et al. 1997; Fellers 2007), during which the dimensional change of a paper sheet due to relative humidity (RH) variations is measured. However, during inkjet printing, liquid water is introduced to the material, resulting in *hydro*-expansion of the paper, which, as shown in Larsson et al. (2009a, b), results in significantly different dimensional changes.

Measurement of the *hygro*-expansion is typically preferred over *hydro*-expansion because in the former, the moisture content (*MC*) can be varied in a (slow) gradual manner, whereas for *hydro*-expansion achieving homogeneous wetting of the sheet is challenging (Larsson et al. 2009a, b). During *hygro*-expansion measurements, no excess water is present, enabling better fiber and sheet surface characterization and full-field monitoring. Moreover, the geometry is better preserved during *hygro*-expansion, as inter-fiber bonds remain stable and out-of-plane deformations are less likely to occur due to a more homogeneous *MC* distribution, thereby enabling easier quantification of the in-plane expansion. Hence, *hygro*-expansion is usually applied for studying the (continuous) transient dimensional change of paper sheets (Salmén et al. 1985; Uesaka et al. 1992; Niskanen et al. 1997; Fellers 2007; Larsson and Wågberg 2008; Vonk et al. 2023d), and its micro-constituents, including fibers (Meylan 1972; Joffre et al. 2016; Vonk et al. 2021). In contrast, the time-dependent spectrum of the transient *hydro*-expansion of fibers has not yet been reported in the literature. On the one hand, all (transverse) fiber shrinkage measurements were performed from wet to dry in one or a few discrete steps (Page and Tydeman 1963; Tydeman et al. 1966; Weise and Paulapuro 1995). On the other hand, Larsson et al. (2009a, 2009b) did achieve small continuous *MC* changes (similar to traditional *hygro*-expansion experiments) for handsheets (using water spraying techniques). However, in contrast to *hygro*-expansion experiments, introducing liquid water to a paper sheet can quickly maximize the *MC*, similar to the one-step fiber *hydro*-expansion tests in Page and Tydeman (1963) Tydeman et al. (1966), and Weise and Paulapuro (1995). It is thought that characterization of the continuous transient *hydro*-expansion behavior of individual fibers while maximizing the *MC*, up to full water immersion, may reveal mechanisms at high *MC* levels that have not yet been studied. Elucidating such mechanisms is not only important for inkjet printing, but also essential for paper making, during which the *MC* remains high.

Paajanen et al. (2022) showed that during single fiber *hygro*-expansion up to a RH of 90%, the hemi-cellulose inside the fibers softens between 40 and 60% RH, whereas the cellulose micro-fibrils swell between 55 to 95%. In Vonk et al. (2021, 2023d) the transient dimensional changes accompanying these phenomena during

hygro-expansion (between 30 and 95% RH) was characterized, revealing curves which are similar to conventional sorption isotherms (Fellers 2007; Paajanen et al. 2022). However, characterization of the dimensional stability of paper sheets above *MC* levels associated with 95% RH remains undiscovered. Additionally, according to Salmén et al. (1987), at these high *MC* levels, phenomena occur that strongly affect the dimensional stability of the paper sheet.

As generally known, restrained dried (RD) paper yields a significantly lower *hygro*-expansion than freely dried (FD) paper (Salmén et al. 1987; Uesaka et al. 1992; Larsson and Wågberg 2008; Urstöger et al. 2020; Vonk et al. 2023d). Salmén et al. (1987) stated that during the paper formation process when the paper is fully saturated, the so-called "dislocated regions", which make up ~50% of the cellulose micro-fibrils, are soft and stretched through the restrained drying procedure, but subsequently hardened during drying from a "wet" to a 90% RH state (Agarwal et al. 2013). For RD paper, during the restrained drying process, the cellulose molecules in the "dislocated regions" are prevented from contracting and therefore stretch and align. The aligned molecular configuration hardens, resulting in a largely reduced swelling of RD fibers when subjected to a *MC* increase. In contrast, for FD handsheets, the cellulose molecules in the "dislocated regions" contract during drying, retaining its (more or less) amorphous configuration, resulting in a larger *hygro*-expansion of FD fibers. The lower *hygro*-expansivity of RD compared to FD fibers (between 30 and 90% RH) was confirmed in Vonk et al. (2023d) and Vonk et al. (2023c), and it was indirectly shown (for hardwood fibers) that indeed the *hygro*-expansion along the micro-fibrils was lower for RD fibers. Furthermore, the alignment of the "dislocated cellulose regions" due to an external force was confirmed using molecular dynamics simulations in (Khodayari et al. 2020). However, the dimensional change of FD and RD fibers and sheets inside the critical region in between 95% RH and fully wet remains untested, as is the influence of the accompanying softening and alignment of the "dislocated cellulose regions" in the micro-fibrils (Salmén et al. 1987; Khodayari et al. 2020).

Therefore, the goal of this work is to investigate the transient *hygro*- and *hydro*-expansion of paper fibers and sheets, specifically in the region above 95% RH and the fully wet state, and the effect of restrained drying. Vonk et al. (2023c) serves as a basis, in which the *hygro*-expansion of single fibers was tested before and after full water immersion, i.e. maximum *MC*. The purpose there was to test if RD fibers are able to "transform" into FD fibers upon water immersion, however, the transition from *hygro*-expansion to full wetting and back was not studied in detail. The purpose of this work is to accurately measure the continuous expansion from the *hygro*-expansion regime into the *hydro*-expansion (full wetting) regime as well as the reversed transition, and do this for both handsheets and fibers extracted from these handsheets, for FD and RD, hardwood (HW) and softwood (SW).

Additionally, this work aims to predict the sheet scale *hygro*- and *hydro*-expansion using a dedicated bi-layer laminate model and asses the predictions compared to the experimental sheet expansions. Various advanced models have been proposed in the literature to predict the sheet *hygro*-expansion from fiber characteristics, e.g. 2D fiber bond and homogenized network models (Bosco et al. 2015a, b, 2017a, b), XFEM fiber models (Samantray et al. 2020), and 3D discrete network models

(Motamedian and Kulachenko 2019; Brandberg et al. 2020). However, quasi-3D characterization of orthogonal inter-fiber bonds in Vonk et al. (2024) will show that a simple analytical bi-layer laminate model suffices to accurately predict the bending deformation of the bonded area, due to the *hygro*-expansion differences of the two fibers. More insight can be gained when a set of measurements can be reproduced with a model containing only these essential ingredients. Therefore, here, the bi-layer laminate model will be extended to predict the sheet-scale *hygro*-expansion.

The paper is structured as follows. First, the *hygro*-expansion of fibers and sheets presented in Vonk et al. (2023c) is briefly reviewed. Then, a novel sheet-scale *hydro*-expansion measurement setup is presented which enables loading FD and RD, HW and SW handsheets from dry to fully saturated using liquid water, while tracking the associated dimensional changes. Next, a recently-developed, full-field fiber-scale *hygro*-expansion method, based on global digital height correlation (GDHC), has been extended to track the transient evolution of the longitudinal, transverse, and shear strains of individual fibers up to the full wetting regime. This enables, for the first time, to monitor the complete time-dependent spectrum of the transition from *hygro*- to *hydro*-expansion of single fibers. With this new method, the transient *hydro*-expansion of fibers extracted from the same handsheets as tested during the sheet-scale *hydro*-expansion experiments is characterized. Collectively, enabling comparison of the *hygro*- and *hydro*-expansion of the fibers and sheets. Finally, an analytical model is derived and the *hygro*- and *hydro*-expansion predicted from the experimental fiber characteristics are compared to the sheet-scale experiments.

Materials and methods

The sheet-scale *hygro*-expansion and fiber-scale *hygro*- and *hydro*-expansion measurements are conducted using the recently-developed, advanced image correlation methods presented in Vonk et al. (2023c). Here, only the main aspects are therefore recalled. An experimental overview of all fibers and sheets of which the *hygro*- and *hydro*-expansion is characterized is given in Table 1.

Table 1 Total amount of samples tested samples which are the same for *hygro*- and *hydro*-expansion

FD	Sheets	Fibers
HW	2	5
SW	2	10
RD	Sheets	Fibers
HW	2	9
SW	2	10

Handsheet preparation and hygro-expansion test method

FD and RD, HW and SW handsheets of ∼60 g/m^2 were produced from unbeaten, bleached HW (Eucalyptus) and SW (mixture of Spruce and Pine) kraft pulp ($\kappa < 2$). The handsheets are cut to sheets of 6×6 cm, and a random speckle pattern was applied to every handsheet using charcoal sticks, which is required for the Global Digital Image Correlation (GDIC) algorithm to enable identification of the in-plane *hygro*-expansion.

The paper sheet-scale *hygro*-expansion was subsequently monitored by applying the novel method proposed in Vonk et al. (2023d), during which each handsheet was subjected to six linearly increasing RH cycles from 30–90–30%, with a slope of 1%/min. The collected images (obtained once every two minutes) are correlated using a GDIC framework with linear shape functions to obtain the evolution of the displacement field, which is converted to a strain measure (*hygro*-expansion) (Neggers et al. 2016). Two FD and RD, HW and SW handsheets were characterized each.

A novel sheet-scale hydro-expansion method

A novel setup, displayed in Fig. 1, is developed to characterize the *hydro*-expansion of the same handsheets as used for the *hygro*-expansion. The speckled handsheets are cut (halved) to strips of 6×3 cm, and clamped by a universal tensile tester as explained below, which is located in a controlled climate of 50% RH and 23 °C. To initiate the *hydro*-expansion, a thermo-electric cooling (Peltier) element is located ∼ 0.5–1 mm from the back of the paper sheet, as shown in Fig. 1, generating condensation when the Peltier element's temperature ($T_{Peltier}$) drops below the dew point temperature (T_{dew}), which is ∼13 °C at 50% RH. Therefore, to initiate the wetting cycle, $T_{Peltier}$ is lowered from 23 to 4 °C in ∼15 min, as displayed in Fig. 1. The sheet first only exhibits *hygro*-expansion, because insufficient condensation is formed to initiate *hydro*-expansion. After ∼10 min, condensation becomes large enough, i.e. ∼1 mm, such that droplets become visible, yet the *hydro*-expansion already initiated before this. $T_{Peltier}$ of 4 °C is chosen to generate the highest rate at which the water is introduced to the sheet, while not freezing the water due to possible temperature fluctuations. $T_{Peltier}$ is maintained at 4 °C for 120 min, which was sufficient to fully saturate the handsheet, as will be shown below. Afterwards, the Peltier element is shut off, through which $T_{Peltier}$ rapidly increases to 23 °C, hence initiating the drying period. Drying takes 60 min, which was sufficient to recover an equilibrium *MC*.

While $T_{Peltier}$ is altering, the handsheet surface is monitored every 10 s using a camera setup, and the transient handsheet *hydro*-expansion is obtained by correlating the images using the same GDIC algorithm as used for the handsheet *hygro*-expansion experiments. Note that due to the introduction of water, the brightness and contrast of the sheet surface strongly deteriorates, resulting in convergence issues in the GDIC. This was remedied by (i) adding an extra degree of freedom to the shape functions used in the GDIC, to shift the gray value spectrum of the deformed image to match the undeformed image, similar to Vonk et al. (2023a), and (ii) adopting a so-called incrementally 'updated' GDIC algorithm, in which each deformed image is correlated with its previous image instead of with the first image.
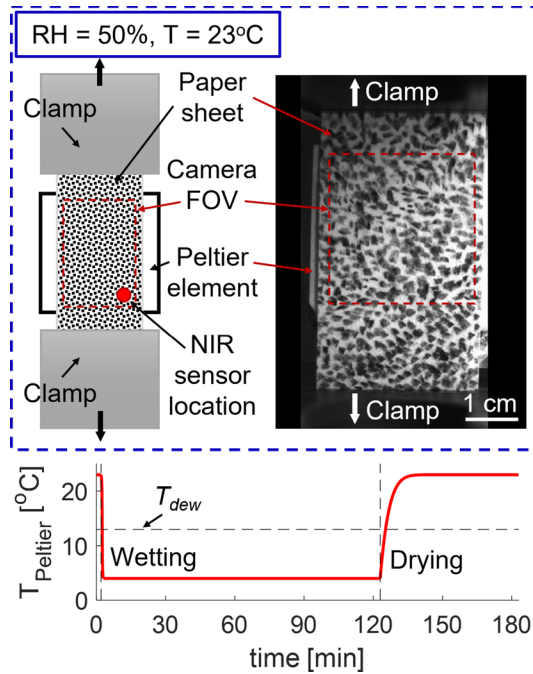
Fig. 1 The novel paper sheet-scale *hydro*-expansion setup, in which the paper sheet is clamped in a universal tensile tester to maintain a flat paper surface inside a 50% and 23 °C climate. A Peltier element is located behind the paper sheet to cool down the handsheet, triggering condensation, consequently initiating *hydro*-expansion. The patterned handsheet surface is captured by a camera, of which the images are correlated using a GDIC algorithm to obtain the transient deformation. $T_{peltier}$ is lowered to 4 °C, which is maintained for 120 min (wetting period) to attain full saturation. Afterwards, the Peltier element is shut off and $T_{peltier}$ rapidly increases to 23 °C (drying period), during which the handsheet is stabilized in 60 min. A near infrared sensor (NIR) is used to determine the average *MC* of the handsheet at the specified position within the area of the Peltier element

Furthermore, throughout the experiment, the sheet is subjected to a constant force of 0.2 N, which is sufficient to straighten the paper sheet to minimize out-of-plane displacements, without inducing significant irreversible deformation. These out-of-plane displacements would otherwise induce artificial strains that are relatively large compared to the small strains expected during *hydro*-expansion. Note that due to the applied force, the swelling becomes slightly anisotropic, which however is outweighed by the large strain errors that would result from out-of-plane deformations in case if no force was applied. To minimize the influence of the tensile strain, the strain in horizontal (free) direction is analyzed.

Finally, a near infrared (NIR) sensor (*FIBRO MCA 1410, FIBRO System AB, Hägersten, Sweden*) is used to determine the average *MC* of a discrete spot at the paper surface which lies within the Peltier element, as indicated in Fig. 1. Note that only the *MC* of this discrete spot is registered and not the *MC* of the full paper sheet. To calibrate the NIR sensor, the tested sheets were fully saturated in water

and subsequently dried on a scale (resolution: 10^{-4} g) in a 50% RH and 23 °C environment, while the transient NIR sensor output voltage and the handsheet weight are logged. Important to note is that output of NIR sensors are very sensitive to the distance and angle at which the sensor is aimed at the specimen. For example, the *MC* changed from 8% to 10% when the pointing angle was changed from 45° to 70° at a fixed distance. To minimize errors due to sample movement, the calibration and the *hydro*-expansion experiments were performed sequentially without disassembling the setup. To maximize the surface of the NIR dot on the paper sheet, an angle of 70° was chosen, and the distance was fixed at 35 mm as the signal-to-noise ratio was found to be best at this distance. care has been taken to find a NIR sensor position. After drying, the dry weight of the paper was obtained by complete drying at 105 °C, similar to Larsson et al. (2009a). To ensure the absolute dry weight, a total drying time of 4 h was used, as mass monitoring during drying revealed that the equilibrium *MC* was reached after 1–2 h. Combined, a linear trend was obtained between the NIR output voltage and *MC*.

Preparation and hygro-expansion approach of the single fibers

From the remainder of the handsheets five FD and nine RD HW fibers as well as ten FD and RD SW fibers were extracted. The fibers are prepared and tested following the method proposed by Vonk et al. (2020). First, the fibers are clamped onto a glass slide using two nylon wires to minimize rigid body translation, needed to keep the fiber in the microscope's field-of-view. Then, a 500 nm particle pattern is applied to the fiber using a dedicated mistification setup (Shafqat and Hoefnagels 2021), which is essential for the GHDC.

The fiber *hygro*-expansion is characterized by changing the surrounding RH, while the fiber topography is captured with an optical profilometer using vertical scanning interferometry mode (*Bruker NPFlex*) during swelling and shrinkage. The topographies are subsequently correlated using the GDHC algorithm to determine the longitudinal, transverse and shear surface strain fields during *hygro*-expansion.

The prepared fiber specimens are mounted in a cooling stage, enabling a controlled temperature (*T*) close to the specimen, which is essential for realizing *hydro*-expansion, as will be discussed below. Each fiber was subjected to two linearly increasing RH cycles from 30–90–30% (cycle 1–2, *hygro*-expansion) at 23 °C, as shown in Fig. 2, after which a wetting cycle initiates (*hydro*-expansion). Note that all fibers were subjected to two 30–90–30% RH (*hygro*-expansion) cycles after the wetting cycle during the experiments discussed in Vonk et al. (2023c), which are outside the scope of this work and are not discussed here.

Fiber hydro-expansion approach

The full-field fiber *hydro*-expansion is characterized within the same experiment as the full-field fiber *hygro*-expansion, as displayed in Fig. 2. The fibers are subjected to a wetting cycle, during which the *MC* is maximized. This is achieved by lowering the specimen temperature (*T*) to 15 °C and increasing the RH set-point to 95%,

Fig. 2 *hygro-* and *hydro-* expansion of fibers extracted from the FD and RD, HW and SW handsheets. After the *hygro*-expansion cycles (cycles 1–2, 30–90–30% RH), a wetting cycle is initiated during which the temperature of the fiber's substrate (T) and the RH are altered to generate condensation, as shown in topographies 2-4, consequently realizing fiber *hydro*-expansion. The *RH* and T trajectories are different for HW and SW, i.e. for HW, T is lowered at low RH after which the RH is raised to high level, resulting in some droplets touching the fiber at the end of the wetting cycle (topography 2), whereas no droplet formation was visible when the high RH is reached (topography 1). For SW, T is lowered while the RH was already at high level, resulting in an increased amount of droplets that touch the fibers (topography 3), however, these droplets grow out to a complete liquid front that runs over the fiber (topography 4), in contrast to the HW approach
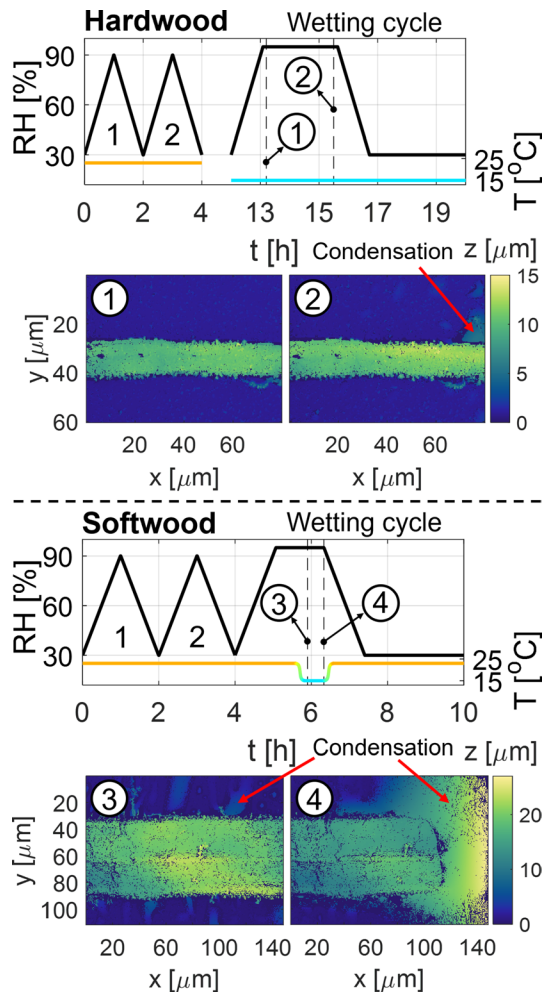

and locally above (Fellers 2007), triggering condensation ($T_{dew} \approx 22\,°C$) at the fiber, realizing *hydro*-expansion. The wetting cycle is, however, different for HW and SW, as visible in the trajectories given in Fig. 2. The reason behind this is that larger amount of condensation was required for the SW fibers (and possibly higher *MC* levels) to understand the results presented in Vonk et al. (2023c), in which a more elaborate argumentation is given.

For the wetting cycle of the HW fibers, T is decreased to 15 °C and stabilized at 30% RH for 8 h, before the wetting cycle initiates. The fiber surface is not monitored during this 8 h, but, respectively, the last and first topography of the *hygro*-expansion cycles and the wetting cycle are correlated to correct for possible strains. The RH is subsequently linearly increased from 30–95% (slope of 1%/min), and the 95% RH set-point is kept constant for 3 h. Visible condensation only starts to form at the end of the high RH period (topography 2), whereas no condensation was visible at

the start (topography 1). During drying, the RH is linearly lowered to 30% and is kept constant for 3 h or longer until no condensation was visible anymore inside the climate chamber, and attain the same fiber state before and after the wetting cycle.

For the wetting cycle of the SW fibers, the RH is first linearly increased to 95% and kept constant for 30 min, after which the temperature is lowered to 15 °C in approximately 15 min. This SW approach enabled the formation of an increased amount of (uncontrollable) condensation compared to the HW approach, which formed right after the change in T (topography 3). The length of the wetting cycle varies per fiber, because T and RH are simultaneously returned to their original value of, respectively, 23 °C and 30% to counter the droplet formation when the condensation starts covering the fiber surface (topography 4), making the GDHC impossible. Again the experiment was stopped when no more condensation was visible. The SW approach generating significantly more and quicker condensation may be because the fiber resides in 95% RH, which, upon cooling, directly condensates. Whereas for the HW approach, the condensation generation already occurred at lower RH levels

Fig. 3 Schematic representation of the bi-layer laminate model used to predict the sheet-scale expansion (ϵ_s) from the experimentally obtained fiber characteristics. The model consists of two orthogonal bonded fibers, in which the sheet expansion (ϵ_s) is a combination of the longitudinal fiber strain (ϵ_{ll}) in the freestanding arms, and the strain in the bonded area (ϵ_b), which are weighted by the free fiber length ratio (η) given by $l_f/(l_f + l_b)$
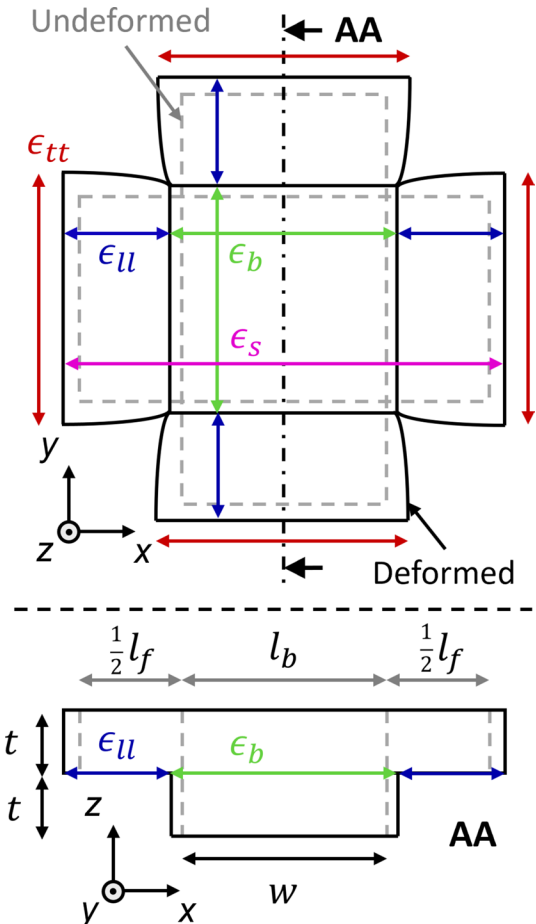
and far from the fiber, because the humidifier's flow first passes the edge of cooling element (where the condensation starts to form) and feedback RH/*T* sensor before reaching the fiber. In the following, for SW, the point at which *T* is lowered up until the point where *T* is increases again will be called the wetting period, and from there onward is called the drying period, as annotated in Fig. 2.

Inter-fiber bond model

A schematic representation of the proposed inter-fiber bond model used to predict the sheet-scale *hygro*- and *hydro*-expansion from the experimentally obtained fiber *hygro*- and *hydro*-expansion characteristics is given in Fig. 3. This model is based on a recently-developed inter-fiber model which describes the deformation in the bonded area of isolated inter-fiber bonds Vonk et al. (2024). The model, assuming a linear deviation of the strain through the thickness of the bonded area, predicts the strain curves through the thickness of the bond, and out-of-plane bending deformation. In Vonk et al. (2024), a good match between this inter-fiber bond model and the experiments was found. Thereby revealing that, even though various non-linear effects are known to occur in the bonded area, a relatively simple model can capture the complex deformation of the bonded area. In order to capture the full mechanics of the bonded area, more elaborate modeling approaches, like Finite Element Modeling, are required. Here, this model is adapted to predict sheet-scale expansion, with the main difference that the bending deformation is restricted to be zero, as bonds inside paper sheets are expected to be heavily constrained by neighboring fibers. Please note that the objective of this model is not to yield high quantitative predictive accuracy. Instead, it is a simplistic model that qualitatively encapsulates the primary effects occurring in the bonded area, while ideally yielding quantitative results that align appropriately within the expected range, which will be displayed below.

The sheet-scale expansion (ϵ_s) is composed of the longitudinal fiber expansion in the freestanding arms (ϵ_{ll}), and the bond strain (ϵ_b), which results from the competition between the ϵ_{ll} of the first fiber and the transverse fiber expansion (ϵ_{tt}) of the second fiber. ϵ_{ll} and ϵ_b are scaled via the free fiber length ratio (η), i.e.:

$$\epsilon_s = \eta \epsilon_{ll} + (1 - \eta)\epsilon_b. \tag{1}$$

Here, η equals $l_f/(l_f + l_b)$, in which l_f and l_b are, respectively, the unbonded and bonded fiber length. To determine ϵ_b, in Vonk et al. (2024) it will be shown that the bending deformation in the bonded area of isolated inter-fiber bonds is accurately described by a bi-layer laminate model based on classical laminate theory for thin plates (Pister and Dong 1959; Reissner and Stavsky 1961). The rigorous derivation towards *hygro*-expansion can be found in Vonk et al. (2024). This model considers a linear variation of the in-plane strain components through the thickness coordinate of the bond (z), i.e. the strain profile in horizontal (ϵ_{xx}) and vertical direction (ϵ_{yy}), see Fig. 3 for the directions of *x*, *y*, and *z*, is given by:

$$\epsilon(z) = \epsilon_0 + \kappa z, \tag{2}$$

in which ϵ_0 is the strain value at the interface between the two fibers, and κ is the curvature. However, inside a paper sheet, the bending deformation is expected to be low due to the constraining neighboring fibers. Therefore, eliminating bending from the bi-layer model provides an estimate of the strain in the bond located inside a paper sheet. Then Eq. 2 simplifies to:

$$\epsilon(z) = \epsilon_0. \tag{3}$$

Assuming two perpendicularly bonded fibers with equal characteristics, in terms of swelling (ϵ_{ll} and ϵ_{tt}), geometry [thickness (t), width (w)], and mechanical properties (E, v), and free expansion ($F = M = 0$), the inter-fiber bond strain (ϵ_b) reduces to:

$$\epsilon_b = \frac{C_{11}\epsilon_{ll} + (C_{12} + C_{22})\epsilon_{tt}}{C_{11} + 2C_{12} + C_{22}},$$

$$\text{with,} \quad C_{11} = \frac{E_l}{1 - v_{lt}v_{tl}}, \quad C_{12} = \frac{v_{tl}E_l}{1 - v_{lt}v_{tl}}, \text{ and } \quad C_{22} = \frac{E_t}{1 - v_{lt}v_{tl}}, \tag{4}$$

in which E_l and E_t are, respectively, the longitudinal and transverse stiffness, and v_{lt} and v_{tl} the Poisson's ratios. Note that due to the equal fiber dimensions, and the free expansion, Eq. 4 does not contain any geometrical parameters. Moreover, Eq. 4 reveals that ϵ_b does not depend on the absolute value of E_l and E_t, but only the fiber stiffness ratio E_t/E_l.

Using Eq. 4, the sheet-scale expansion can directly be predicted, upon inserting the experimentally obtained fiber swelling properties, i.e. ϵ_{ll} and ϵ_{tt}, assuming a free fiber length of ~50% (Wernersson et al. 2014; Borodulina et al. 2016; Urstöger et al. 2020), and adopting the fiber stiffness characteristics from the literature with $v_{lt} = v_{tl}$ equal to 0.022 (Magnusson and Östlund 2013; Brandberg et al. 2020; Czibula et al. 2021). E_t/E_l is different for FD and RD, HW and SW fibers (Jentzen 1964), therefore a range of values for E_t/E_l between 6 and 11 is studied here, covering the relevant range of values found in the literature (Magnusson and Östlund 2013; Brandberg et al. 2020; Czibula et al. 2021).

Results and discussion

Many different strain quantities are compared in this paper, therefore the following notation is consistently adopted in this work: $\epsilon_{s/ll/tt/lt}^{\gamma/\delta+/-}$, in which superscript γ versus δ denote *hygro-* versus *hydro-*expansion [referring to the Greek *υγροσκοπικός* (*hygro*scopic) and *υδροσκοπικός* (*hydro*scopic)]; superscript $+$ versus $-$ denote, respectively, wetting versus drying; and subscript $_s$ denotes sheet-scale values, whereas the fiber-scale strain components are denoted with subscripts $_{ll}$, $_{tt}$, and $_{lt}$, corresponding to, respectively, longitudinal, transverse and shear strain. All of the above strains notations are variables, whereas the absolute strain changes during

Fig. 4 **a** The transient longitudinal (ϵ_{ll}), transverse (ϵ_{tt}), and shear strain (ϵ_{lt}) during *hygro-* (cycles 1–2) and *hydro-*expansion (wetting cycle) of a FD SW fiber. The strains change during drying from 90 to 30% (*hygro-*expansion, cycles 1–2), annotated as $\underset{\Delta}{\epsilon}_{ll}^{\gamma-}$, $\underset{\Delta}{\epsilon}_{tt}^{\gamma-}$, and $\underset{\Delta}{\epsilon}_{lt}^{\gamma-}$ are extracted. **b** Four topographies, as annotated in the ϵ_{tt} curve (**a**), are used to display the phenomena during wetting of the SW fibers, in order to better understand the *hydro-*expansion response. Note that topography 3 and 4 are given in Fig. 2. The strain changes during the wetting cycle for wetting and drying, respectively, $\underset{\Delta}{\epsilon}_{ll}^{\delta+}$, $\underset{\Delta}{\epsilon}_{tt}^{\delta+}$, and $\underset{\Delta}{\epsilon}_{lt}^{\delta+}$, and $\underset{\Delta}{\epsilon}_{ll}^{\delta-}$, $\underset{\Delta}{\epsilon}_{tt}^{\delta-}$, and $\underset{\Delta}{\epsilon}_{lt}^{\delta-}$, are also extracted. The crosses (at $t = 9$ hours) in (**a**) indicate the fiber strain after equilibrating the RH and T to, 30% and 23 °C respectively, equal to the start of the experiment (at $t = 0$ hours)


(a) Hygro- and hydro-expansion of a FD SW fiber
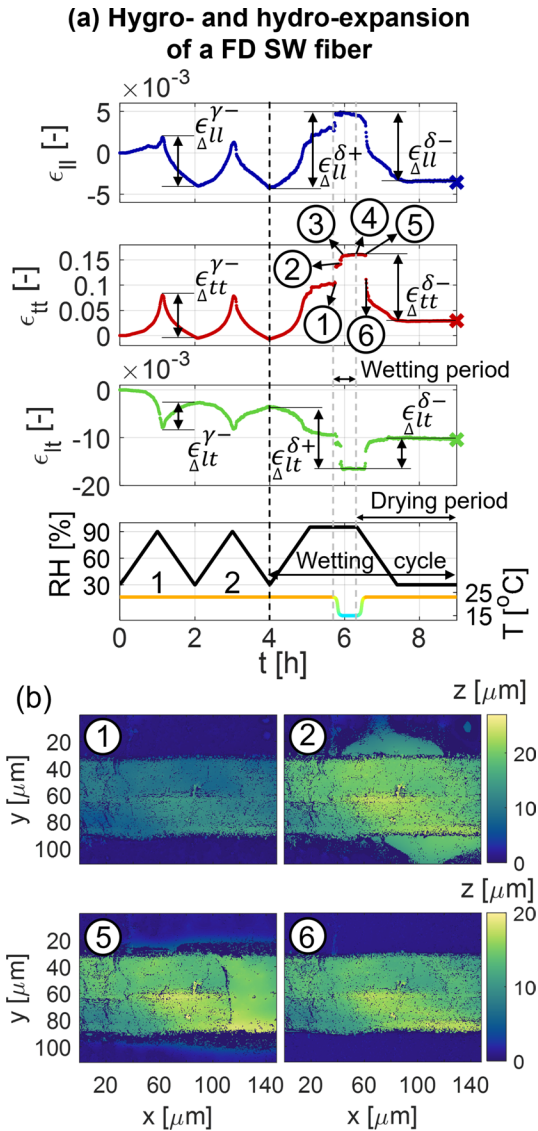
wetting and drying, which are constant values, are denoted using a Δ under the strain symbol, i.e. $\underset{\Delta}{\epsilon}$. Finally, a bar over the strain symbol, i.e. $\bar{\epsilon}$, denotes the average value of a measurement ensemble.

Fiber and sheet hygro-expansion

Figure 4a shows a typical fiber-scale measurement of the longitudinal, transverse and shear strain of a FD SW fiber, monitored during 2 *hygro-*expansion cycles and

Fig. 5 The average **a** longitudinal and **b** transverse shrinkage, and **c** shear strain change during drying from 90 to 30% RH of cycles 1–2 of all fibers, i.e. $\bar{\epsilon}^{\gamma-}_{\Delta ll}$, $\bar{\epsilon}^{\gamma-}_{\Delta tt}$, and $\bar{\epsilon}^{\gamma-}_{\Delta lt}$, including their standard deviation. The average handsheet shrinkage ($\bar{\epsilon}^{\gamma-}_{\Delta s}$ given in Table 3) is added to the $\bar{\epsilon}^{\gamma-}_{\Delta ll}$ plot to compare

Fiber and sheet hygro-expansion
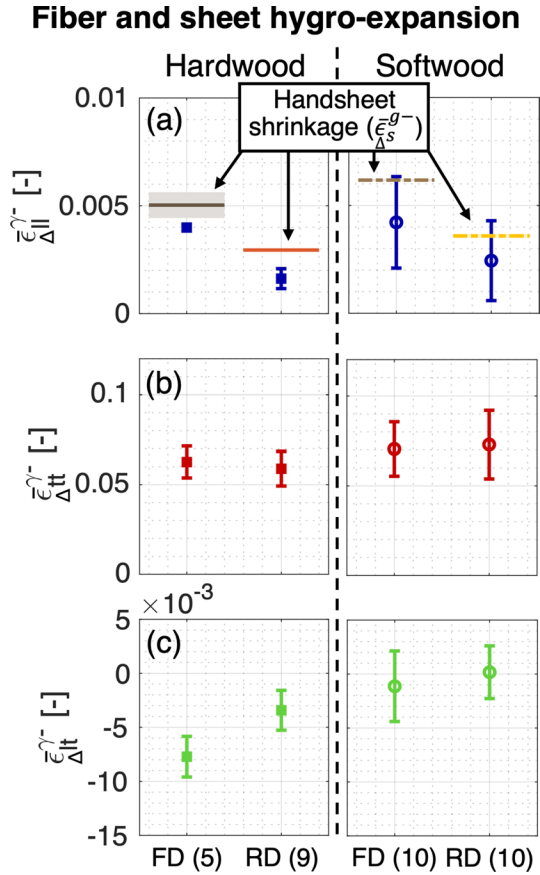
1 *hydro*-expansion cycle (with corresponding topographies in b). For now, only the *hygro*-expansion in Fig. 4 is discussed. The fibers' longitudinal and transverse shrinkage, and shear strain change during drying from 90 to 30% RH (*hygro*-expansion) for cycles 1–2, i.e. $\epsilon^{\gamma-}_{\Delta ll}$, $\epsilon^{\gamma-}_{\Delta tt}$, and $\epsilon^{\gamma-}_{\Delta lt}$, as annotated in Fig. 4, are extracted for each fiber. The average shrinkage considering cycles 1–2 of all fibers, i.e. $\bar{\epsilon}^{\gamma-}_{\Delta ll}$, $\bar{\epsilon}^{\gamma-}_{\Delta tt}$, and $\bar{\epsilon}^{\gamma-}_{\Delta lt}$, including their standard deviation, are displayed for FD and RD, HW and SW in Fig. 5, and given in Table 2.

From the transient sheet-scale *hygro*-expansion curve of two FD and RD, HW and SW handsheets, the shrinkage for each drying slope from 90 to 30% RH is extracted. The average shrinkage considering both sheets per handsheet type ($\bar{\epsilon}^{\gamma-}_{\Delta s}$), including its standard deviation are plotted in the top row of Fig. 5, and given in Table 3.

Regarding the handsheet *hygro*-expansion, Fig. 5 shows that $\bar{\epsilon}^{\gamma-}_{\Delta s}$ is significantly larger for the FD compared to RD, similar to the literature (Uesaka et al. 1992; Nanko and Wu 1995; Larsson and Wågberg 2008; Urstöger et al. 2020; Vonk et al. 2023d), and $\bar{\epsilon}^{\gamma-}_{\Delta s}$ of the SW handsheets is slightly larger than for their

HW counterparts. Regarding the fiber *hygro*-expansion, $\bar{\epsilon}_{\underset{\Delta}{ll}}^{\gamma-}$ is also significantly larger for FD compared to RD, similar to the corresponding handsheets. This, combined with the fact that the longitudinal fiber swelling strongly affects the dimensional stability of paper (Uesaka 1994; Brandberg et al. 2020; Motamed-ian and Kulachenko 2019), indicates that the sheet-scale *hygro*-expansion differences between FD and RD are predominantly caused by the differences at the fiber level, in contrast to reports in the literature attributing the FD/RD differences to geometrical differences in the inter-fiber bonds (Uesaka 1994; Larsson and Wågberg 2008). The importance of the longitudinal fiber *hygro*-expansion is further supported by the observation that, for all handsheets, $\bar{\epsilon}_{\underset{\Delta}{s}}^{\gamma-}$ is only slightly larger than $\bar{\epsilon}_{\underset{\Delta}{ll}}^{\gamma-}$, indicating that the transverse fiber *hygro*-expansion contribution to the sheet scale is small, as observed in the *hygro*-expansion experiments on isolated inter-fiber bonds in Vonk et al. (2024), and models of the network *hygro*-expansion (Motamedian and Kulachenko 2019; Brandberg et al. 2020).

Sheet-scale hydro-expansion

The sheet-scale *hydro*-expansion and *MC* evolution of a FD and RD, HW and SW handsheet during the wetting cycle of the sheet-scale *hydro*-expansion experiments, i.e., respectively, $\epsilon_s^{\delta+}$ and $MC_s^{\delta+}$, are displayed in Fig. 6(a, c). To enable a better comparison between the handsheets, $\epsilon_s^{\delta+}$ and $MC_s^{\delta+}$ are also plotted relative to the
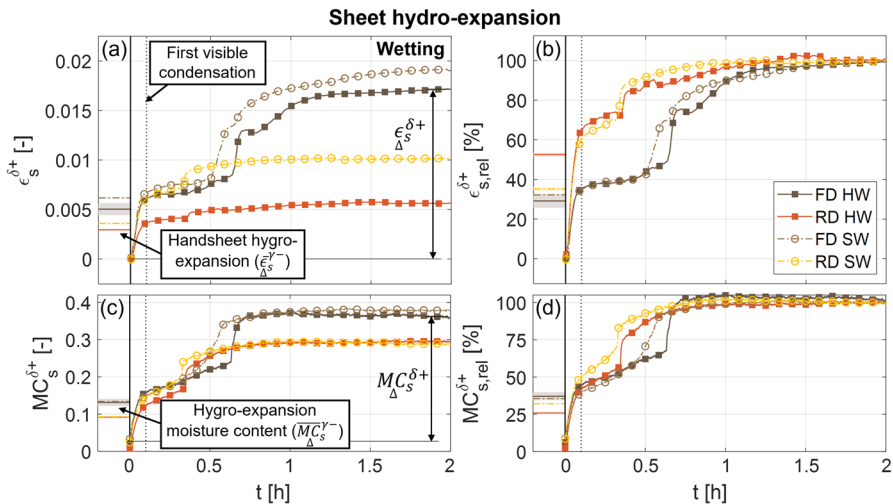

Fig. 6 The transient sheet-scale *hydro*-expansion and *MC* during wetting of the sheet-scale *hydro*-expansion experiment, i.e., respectively, $\epsilon_s^{\delta+}$ and $MC_s^{\delta+}$. $\epsilon_s^{\delta+}$ and $MC_s^{\delta+}$ are divided by, respectively, their maximum value at the end of the wetting cycle (at $t = 2$ hours), to find the $\epsilon_{s,rel}^{\delta+}$ and $MC_{s,rel}^{\delta+}$ curves, enabling a better comparison between the handsheets. The handsheet shrinkage during the *hygro*-expansion experiments ($\bar{\epsilon}_{\underset{\Delta}{s}}^{\gamma-}$ in Fig. 5) and $\bar{MC}_{\underset{\Delta}{s}}^{\gamma-}$ are added to highlight the magnitude differences between the *hygro*- and *hydro*-expansion experiments. The first condensation was visible after 10 min for all handsheets, marked by the dotted line in the figures. The total changes in $\epsilon_s^{\delta+}$ and $MC_s^{\delta+}$, i.e., respectively, $\epsilon_{\underset{\Delta}{s}}^{\delta+}$ and $MC_{\underset{\Delta}{s}}^{\delta+}$, are extracted

Table 2 Average longitudinal ($\bar{\varepsilon}^{\gamma-}_{\Delta ll}$) and transverse shrinkage ($\bar{\varepsilon}^{\gamma-}_{\Delta tt}$), and shear strain change ($\bar{\varepsilon}^{\gamma-}_{\Delta lt}$) considering the drying slopes from 90 to 30% RH of cycles 1–2 (*hygro*-expansion) for five FD and nine RD HW fibers, and ten FD and RD SW fibers, including their standard deviation

FD	$\bar{\varepsilon}^{\gamma-}_{\Delta ll}$ [-]	$\bar{\varepsilon}^{\gamma-}_{\Delta tt}$ [-]	$\bar{\varepsilon}^{\gamma-}_{\Delta lt}$ [-]
HW	0.0040 ± 0.0002	0.0627 ± 0.0089	− 0.0077 ± 0.0019
SW	0.0042±0.0021	0.0705 ± 0.0151	−0.0011 ± 0.0033
RD	$\bar{\varepsilon}^{\gamma-}_{\Delta ll}$ [-]	$\bar{\varepsilon}^{\gamma-}_{\Delta tt}$ [-]	$\bar{\varepsilon}^{\gamma-}_{\Delta lt}$ [-]
HW	0.0016 ± 0.0005	0.0589 ± 0.0096	− 0.0034 ± 0.0018
SW	0.0024 ± 0.0019	0.0729 ± 0.0191	0.0002 ± 0.0024

maximum value found at the end of the wetting period (i.e. at $t = 2$ hours), i.e. $\varepsilon^{\delta+}_{s,rel}$ and $MC^{\delta+}_{s,rel}$ in Fig. 6(b, d). The average sheet-scale shrinkage during *hygro*-expansion ($\bar{\varepsilon}^{\gamma-}_{\Delta s}$), given in Fig. 5a, has been added to the left of the curves for comparison. Additionally, an approximation of the $\bar{MC}^{\gamma-}_{\Delta s}$ is obtained by looking up the $MC^{\delta+}_s$ value corresponding to the $\bar{\varepsilon}^{\gamma-}_{\Delta s}$ value in the $\varepsilon^{\delta+}_s$-$MC^{\delta+}_s$ curve, which are added to the $MC^{\delta+}_s$ plots. Note that this is an approximated $\bar{MC}^{\gamma-}_{\Delta s}$, because MC^{γ}_s was not monitored during the *hygro*-expansion experiments, only during the *hydro*-expansion experiments.

First of all, the novel sheet-scale *hydro*-expansion method is sufficiently robust to characterize the evolution of the sheet expansion from dry to fully wet with high precision, especially considering the large brightness and contrast deterioration of the images during the experiments. This indicates that the adaptations to the GDIC algorithm, described in the methodology, are instrumental. The wetting was achieved relatively uniformly over the paper surface, because no localized hot spots were visible in the converged correlation residual field from the GDHC algorithm. Moreover, $\varepsilon^{\delta+}_s$ and $MC^{\delta+}_s$ display similar curves, indicating that both measurements were performed consistently, because the moisture-induced dimensional change of FD paper should, approximately, depend linearly on the *MC* (Uesaka et al. 1992; Larsson and Wågberg 2008). Furthermore, the handsheets reach an equilibrium much later for wetting than drying due to slower mass transfer during wetting, similar to the sheet and fibers *hygro*-expansion measurements in the literature (Niskanen et al. 1997; Vonk et al. 2021). Finally, note that the sheets first exhibit *hygro*-expansion

Table 3 The average shrinkage ($\bar{\varepsilon}^{\gamma-}_{\Delta s}$) considering the six drying slopes from 90 to 30% RH (*hygro*-expansion) of two FD and RD, HW and SW handsheets, including their standard deviation

| FD	$\bar{\varepsilon}^{\gamma-}_{\Delta s}$ [-]
HW	0.0050 ± 0.0006
SW	0.0062 ± 0.0001
RD	$\bar{\varepsilon}^{\gamma-}_{\Delta s}$ [-]
HW	0.0029 ± 0.0001
SW	0.0036 ± 0.0001

Table 4 The maximum swelling ($\epsilon_{\Delta s}^{\delta+}$) and shrinkage ($\epsilon_{\Delta s}^{\delta-}$) of a FD and RD, HW and SW handsheet during the sheet-scale *hydro*-expansion experiments as annotated in Fig. 6

FD	$\epsilon_{\Delta s}^{\delta+}$ [-]	$\epsilon_{\Delta s}^{\delta-}$ [-]
HW	0.0173	0.0208
SW	0.0192	0.0271
RD	$\epsilon_{\Delta s}^{\delta+}$ [-]	$\epsilon_{\Delta s}^{\delta-}$ [-]
HW	0.0056	0.0144
SW	0.0102	0.0168

before the condensation droplets become visible after approximately 10 min, during which *hydro*-expansion sets in. After this point, most handsheets swell a factor 2 more compared to the final swelling after *hygro*-expansion from 30 to 90% (Fig. 6), whereby both $\epsilon_s^{\delta+}$ and $MC_s^{\delta+}$ converge (approximately) to a plateau value. This indicates that the sheet *hydro*-expansion was successfully characterized in between the 90% RH and the fully saturated regime.

Similar to the sheet *hygro*-expansion experiments (Fig. 5), in the *hydro*-expansion experiments, the FD sheets exhibit a larger $\epsilon_s^{\delta+}$ at the end of the wetting cycle than the RD handsheets, and the SW handsheets swell more than their corresponding HW counterparts. The ultimate swelling resulting from wetting of the *hydro*-expansion cycle, i.e., $\epsilon_{\Delta s}^{\delta+}$ annotated in Fig. 6, is extracted and given in Table 4. Interestingly, the transient $\epsilon_s^{\delta+}$ and $MC_s^{\delta+}$ display significant differences from conventional *hygro*-expansion curves, i.e., all handsheets show an abrupt transition (step) in $\epsilon_s^{\delta+}$ and $MC_s^{\delta+}$ around $t = 0.5$ hours. This step is significantly larger and occurs later for FD compared to the RD handsheets. This step becomes even better visible for the $\epsilon_{s,rel}^{\delta+}$ and $MC_{s,rel}^{\delta+}$ curves. At first glance, it may seem that this step characterizes the transition from *hygro*- to *hydro*-expansion, during which liquid water directly ingresses in the sheet and hence the sheet swells quicker. However, the first water droplets were already visible after 10 min, indicated by the black, dotted line in Fig. 6), and the step occurs much later. Moreover, the FD and RD sheets reveal distinctly different timescales for this step, whereas SW and HW do not show a clear difference, which cannot be trivially explained if the time scale is governed by the absorption of water in the network. Additionally, it is known from literature that the gross network water absorption should occur much faster, i.e. in the order of seconds/minutes (Niskanen et al. 1997; Jajcinovic et al. 2018), which corresponds with the initial increase in $MC_s^{\delta+}$ that occurs within the first 10 min, where the slightly longer timescale is caused by the non-instantaneous temperature drop. Note also that this initial increase occurs with precisely the same timescale for FD and RD and for SW and HW, see Fig. 6 (d), as is to be expected for the uptake of water in the network. The fact that the type of drying process rather than the type of (SW or HW) fibers mainly affects the timescale of the step (which occurs after the initial increase) indicates that the drying process can be a controlling mechanism. Based on this insight, a hypothesis for this process is proposed below, for which the sheet *hydro*-expansion during drying and the fiber *hydro*-expansion need to be rationalized first.

Fig. 7 The transient sheet-scale *hydro*-expansion and *MC* during drying of the sheet-scale *hydro*-expansion experiment, i.e., respectively, $\epsilon_s^{\delta-}$ and $MC_s^{\delta-}$. $\epsilon_s^{\delta-}$ and $MC_s^{\delta-}$ start at 0 to display the shrinkage of the sheet from wet to dry, to assist in the visual comparison of the curves. The negative values of $\underset{\Delta s}{\epsilon}^{\delta+}$ and $\underset{\Delta s}{MC}^{\delta+}$ are added right of the curves to reveal the release of irreversible dried-in strains, showing that MC_s^{δ} at the start and end of the experiment are almost the same ($MC_s^{\delta-} = MC_s^{\delta+}$), which is clearly not the case for ϵ_s^{δ} ($\underset{\Delta s}{\epsilon}^{\delta-} \neq \underset{\Delta s}{\epsilon}^{\delta+}$). The final change in $\epsilon_s^{\delta-}$, i.e. $\underset{\Delta s}{\epsilon}^{\delta-}$, is extracted
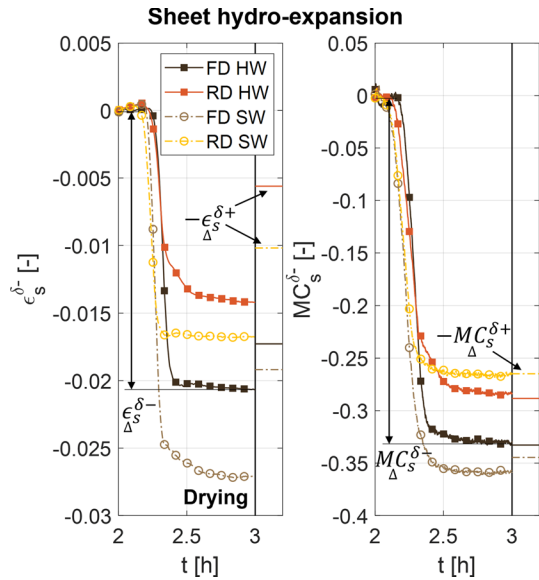
The evolution of the sheet-scale *hydro*-expansion and *MC* during drying of the sheet-scale *hydro*-expansion experiment, i.e., respectively, $\epsilon_s^{\delta-}$ and $MC_s^{\delta-}$, combined with the negative values of $\underset{\Delta s}{\epsilon}^{\delta+}$ and $\underset{\Delta s}{MC}^{\delta+}$ are given in Fig. 7. The final shrinkage after drying, i.e. $\underset{\Delta s}{\epsilon}^{\delta-}$, is extracted and given in Table 4. Similar to the wetting cycles, the RD and HW handsheets shrink less than, respectively, the FD and SW handsheets. Furthermore, all sheets show roughly the same MC_s^{δ} before and after the *hydro*-expansion cycle, indicating that the experiment was conducted properly, such that the wetting and drying strains can be quantitatively compared. Similar to the *hygro*-expansion experiments, the RD handsheets exhibit a larger release of irreversible dried-in strain relative to their swelling cycle ($\underset{\Delta s}{\epsilon}^{\delta-}/\underset{\Delta s}{\epsilon}^{\delta+}$), i.e. for the RD HW and SW sheets, the shrinkage magnitude is, respectively, 2.57 and 1.64 times larger than $\underset{\Delta s}{\epsilon}^{\delta+}$, whereas for the FD HW and SW handsheets, this is only 1.21 and 1.41.

In Vonk et al. (2023c) it was found that the FD fibers exhibit a significantly larger *hygro*-expansivity than the RD fibers, and the RD HW fibers can "transform" to HW fibers exhibiting the *hygro*-expansion characteristics of FD HW fiber, while the RD SW fibers cannot. Considering the sheet-scale shrinkage magnitudes here, the difference between the RD and FD handsheets is much larger for HW than SW, suggesting that the fiber level "transformation" for RD to FD HW fibers also occurs for RD HW sheets. However, note that this sheet-scale "transformation" is not fully effective because the shrinkage of the FD HW handsheet remains larger than the RD HW handsheet in Fig. 7. To test if the "transformation" really occurs at the sheet level, the *hygro*-expansion of the handsheets tested during the *hydro*-expansion experiments should be

Table 5 Average longitudinal and transverse, and shear strain change for wetting and drying during the wetting cycle, i.e., respectively, $\bar\epsilon_{\Delta ll}^{\delta+}$, $\bar\epsilon_{\Delta tt}^{\delta+}$, and $\bar\epsilon_{\Delta lt}^{\delta+}$, and $\bar\epsilon_{\Delta ll}^{\delta-}$, $\bar\epsilon_{\Delta tt}^{\delta-}$, and $\bar\epsilon_{\Delta lt}^{\delta-}$ annotated in Fig. 4, for five FD and nine RD HW fibers, and ten FD and RD SW fibers, including their standard deviation

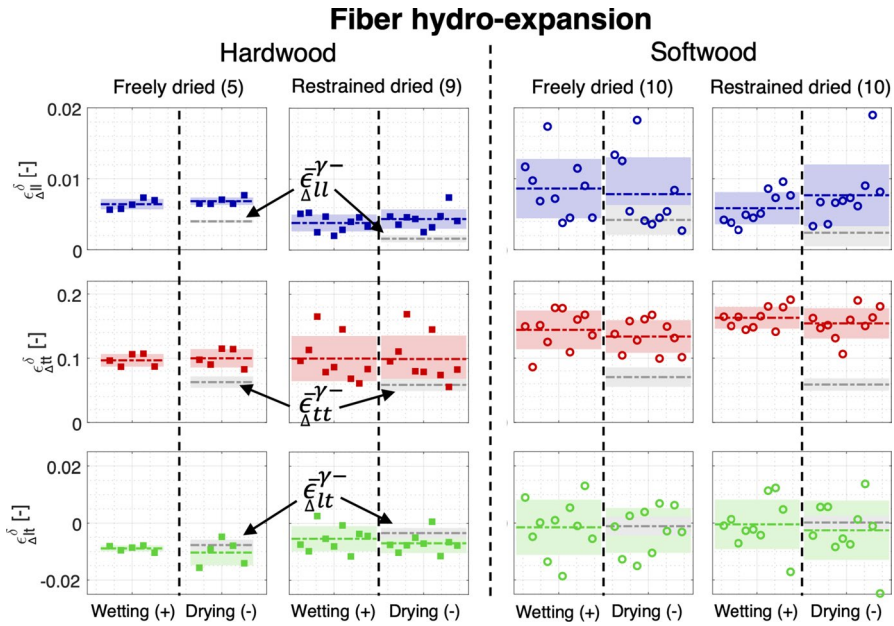| FD	$\bar\epsilon_{\Delta ll}^{\delta+}$ [-]	$\bar\epsilon_{\Delta tt}^{\delta+}$ [-]	$\bar\epsilon_{\Delta lt}^{\delta+}$ [-]	$\bar\epsilon_{\Delta ll}^{\delta-}$ [-]	$\bar\epsilon_{\Delta tt}^{\delta-}$ [-]	$\bar\epsilon_{\Delta lt}^{\delta-}$ [-]
HW	0.0064 ± 0.0007	0.0966 ± 0.0099	− 0.0089 ± 0.0011	0.0068 ± 0.0005	0.0998 ± 0.0144	− 0.0103 ± 0.0045
SW	0.0086 ± 0.0042	0.1441 ± 0.0302	− 0.0015 ± 0.0097	0.0078 ± 0.0052	0.1337 ± 0.0254	− 0.0026 ± 0.0079
RD	$\bar\epsilon_{\Delta ll}^{\delta+}$ [-]	$\bar\epsilon_{\Delta tt}^{\delta+}$ [-]	$\bar\epsilon_{\Delta lt}^{\delta+}$ [-]	$\bar\epsilon_{\Delta ll}^{\delta-}$ [-]	$\bar\epsilon_{\Delta tt}^{\delta-}$ [-]	$\bar\epsilon_{\Delta lt}^{\delta-}$ [-]
HW	0.0038 ± 0.0012	0.0999 ± 0.0352	− 0.0054 ± 0.0045	0.0044 ± 0.0014	0.0992 ± 0.0365	− 0.0070 ± 0.0034
SW	0.0058 ± 0.0023	0.1629 ± 0.0170	− 0.0004 ± 0.0087	0.0077 ± 0.0044	0.1542 ± 0.0237	− 0.0025 ± 0.0104

Fiber hydro-expansion

Fig. 8 The maximum longitudinal, transverse and shear strain changes per fiber for wetting and drying during the wetting cycle annotated as, respectively, $\epsilon_{\Delta ll}^{\delta+}$, $\epsilon_{\Delta tt}^{\delta+}$, and $\epsilon_{\Delta lt}^{\delta+}$, and $\epsilon_{\Delta ll}^{\delta-}$, $\epsilon_{\Delta tt}^{\delta-}$, and $\epsilon_{\Delta lt}^{\delta-}$ in Fig. 4. The colored bands represent the average and standard deviation. The gray bands represent the average strain changes during drying from 90 to 30% RH (*hygro*-expansion experiments) considering cycles 1–2 for all fibers (i.e. $\bar{\epsilon}_{\Delta ll}^{\gamma-}$, $\bar{\epsilon}_{\Delta tt}^{\gamma-}$, and $\bar{\epsilon}_{\Delta lt}^{\gamma-}$, given in Table 2), including their standard deviations

characterized afterwards. Furthermore, as generally known, the elastic stiffness of RD handsheets is larger than FD handsheets (Urstöger et al. 2020; Alzweighi et al. 2021). Hence, to test if not only the *hygro*scopic properties of RD handsheets "transform" after wetting, the elastic stiffness of the FD and RD handsheets before and after the the *hydro*-expansion cycle should be obtained.

Fiber hydro-expansion

Let us remember the combined transient *hygro*- and *hydro*-expansion response of a FD SW fiber given in Fig. 4a. First of all, the fiber swells significantly more during the wetting cycle compared to RH cycles 1–2, indicating that higher *MC* levels are attained. Next, the *hydro*-expansion is initiated just after the *T* is lowered, inducing the tiny droplets observed in topography 1 in Fig. 4b. Interestingly, topography 2 displays a water droplet residing under the fiber, which disappeared in the next topography and did not reappear in the following topographies (topography 3 in Fig. 2), indicating that the fiber was able to fully absorb the (relatively large) droplet. Furthermore, for all SW fibers, the fiber shrinkage is significantly delayed from the RH curve because condensation is present around the SW fibers at the start of the drying period, requiring time to evaporate. During the drying period, the FD SW

Fig. 9 The longitudinal, transverse, and shear strain evolution of **a** four (out of ten) FD and **b** RD SW fibers during the wetting cycle (excluding the drying period), i.e., respectively, $\epsilon_{ll}^{\delta+}$, $\epsilon_{tt}^{\delta+}$, and $\epsilon_{lt}^{\delta+}$. The curves are vertically shifted to start at zero strain for better comparison between the fibers. The RH of the third and fourth RD SW fiber revealed an overshoot to 98% RH when the set-point was supposed to be 95% RH. Consequently, droplet formation was already visible and the fiber exhibited *hydro*-expansion, hence the peaks in the strain curves

(a) Hydro-expansion of FD SW fibers

(b) Hydro-expansion of RD SW fibers
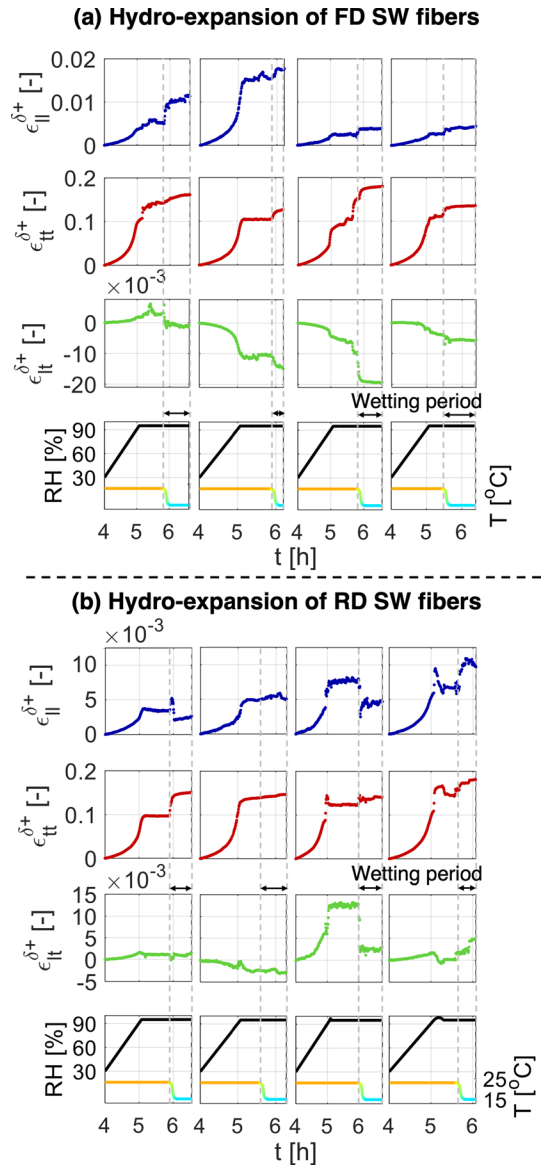
fiber shows a large jump in $\epsilon_{tt}^{\delta-}$, which is less prominently visible for $\epsilon_{ll}^{\delta-}$ and $\epsilon_{lt}^{\delta-}$. All other FD and RD SW fibers displayed similar steps. The formation of a water layer in between the fiber and glass (topography 5) most likely fixates the fiber to the substrate due to capillary forces, similar to Page and Tydeman (1963). This layer disappeared just after the strain jump (topography 6 in Fig. 4). The HW fibers did not show this jump because no water layer was formed in these tests, resulting in introducing less condensation to the HW fibers compared to the SW fibers.
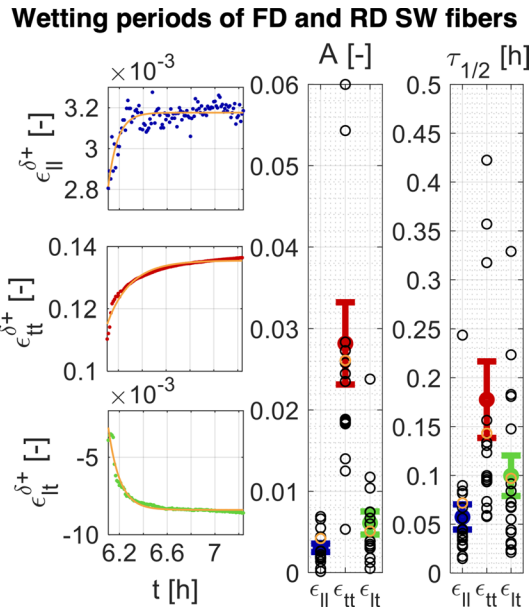
Fig. 10 Strain step amplitude (A) and saturation half-times ($\tau_{1/2}$) of the longitudinal, transverse and shear strain curve of all SW fibers during the wetting period (annotated in the wetting cycle in Fig. 4) after the hypothesized softening of the "dislocated regions" in the cellulose micro-fibrils. A and $\tau_{1/2}$ are obtained by fitting the strain curves using $Ae^{1-\frac{t}{\tau_{1/2}}} + B$, where the constants A and B are given in the ϵ_{ll} plot. In the ensemble plots, the three values plotted in orange open circles correspond to the fits in the three separate strain plots shown on the left, and the black symbols open circles represent the values of the other fibers. The mean values of A and $\tau_{1/2}$ are shown by the solid circles, plotted together with an error bar denoting the standard deviation of the mean

For quantitative comparison, the maximum swelling or shrinkage during the wetting cycle, respectively, $\epsilon_{\Delta ll}^{\delta+}$, $\epsilon_{\Delta tt}^{\delta+}$, and $\epsilon_{\Delta lt}^{\delta+}$, and $\epsilon_{\Delta ll}^{\delta-}$, $\epsilon_{\Delta tt}^{\delta-}$, and $\epsilon_{\Delta lt}^{\delta-}$, as annotated in Fig. 4, are extracted for every FD and RD, HW and SW fiber and separately displayed along with their averages and standard deviations in Fig. 8. The corresponding values of the fiber *hydro*-expansion are also given in Table 5. The fiber shrinkage during the *hygro*-expansion experiments, i.e. $\bar{\epsilon}_{\Delta ll}^{\gamma-}$, $\bar{\epsilon}_{\Delta tt}^{\gamma-}$, and $\bar{\epsilon}_{\Delta lt}^{\gamma-}$ are added, displaying that all fiber strain component magnitudes during the wetting cycle are significantly larger. Furthermore, the average longitudinal shrinkage during drying ($\bar{\epsilon}_{\Delta ll}^{\delta-}$) of the (HW and SW) RD fibers is larger than the average swelling during wetting ($\bar{\epsilon}_{\Delta ll}^{\delta+}$), hence the fiber is shorter after the wetting cycle. This is a logical result, as most fibers were dried under a tensile load, which is released during the wetting cycle. Additionally, this difference complies well with the negative release of longitudinal dried-in strain of the same fibers found in Vonk et al. (2023c). Finally, similar to the *hygro*-expansion given in Fig. 5, the SW fibers display a significantly larger scatter in strain under *hydro*-expansion than the HW fibers, and, similar to *hygro*-expansion (Fig. 5), $\bar{\epsilon}_{\Delta lt}^{\delta}$ of the FD and RD SW fibers remains around zero.

To relate the data to existing works, Tydeman et al. (1966) showed that eleven SW fibers, on average, shrunk 18.36±6.70% in transverse direction from full wet to dry, and Page and Tydeman (1963) showed that a SW fiber shrunk 16% from wet to dry (20% RH), both complying well with the transverse shrinkage of 15.4±2.4% and 13.4±2.5% found for, respectively, the FD and RD SW fibers here. The presented results are, however, different from the transverse shrinkage of around 40% found by Weise and Paulapuro (1995).

To study the evolution of the fiber strain during *hydro*-expansion, the transient *hydro*-expansion during the wetting cycle (excluding the drying period) of four FD and four RD SW fibers is given in Fig. 9. Firstly, the step in strain which stabilizes over time observed during the sheet-scale *hydro*-expansion, is also visible in
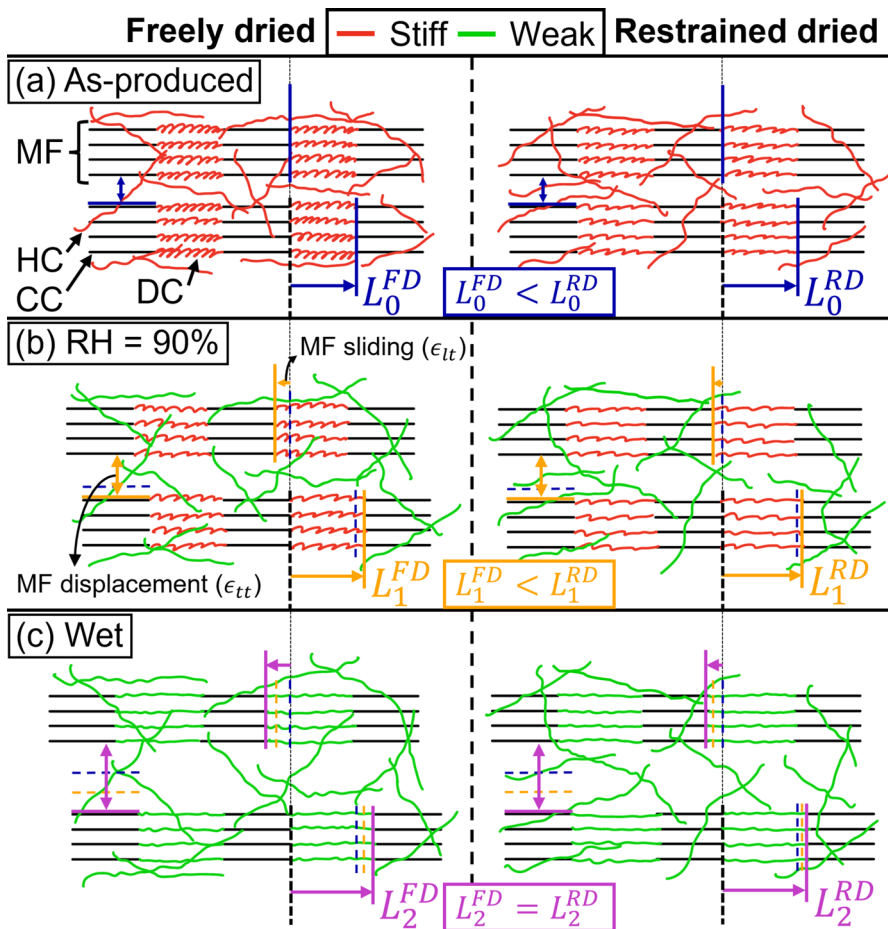
Fig. 11 Schematic representation of the fiber wall structure in as-produced state, 90% RH state, and fully wet state, to support the proposed hypothesis to explain the FD and RD, sheet and fiber, *hygro*-expansion and *hydro*-expansion findings. L = length of the "dislocated cellulose regions". MF = micro-fibril, HC = hemi-cellulose, CC = crystalline cellulose, and DC = "dislocated cellulose"

the transient *hydro*-expansion of all SW fibers during the wetting cycle (more specifically, during the wetting period, as annotated in Fig. 4a). Note that for the fiber experiments it is more difficult to reliably state that this strain step cannot be attributed to the transition between *hygro*- and *hydro*-expansion, unlike for to the sheet-scale *hydro*-expansion experiments. However, small condensation droplets were visible near all fibers before the strain step initiated, suggesting that the fibers were already exhibiting *hydro*-expansion, and a different mechanism drives the observed strain steps, similar to the handsheet *hydro*-expansion observations.

Moreover, the sheet-scale *hydro*-expansion stabilizes much slower than the fibers. This can be explained by the handsheet *hydro*-expansion curve representing the response of all fibers constituting the sheet which are required to equilibrate before the handsheet is in full equilibrium, whereas this is not the case for single fibers. Furthermore, the RD SW fibers display both small positive and small negative steps in $\epsilon_{ll}^{\delta+}$, while the FD SW fibers only display (larger) positive steps in $\epsilon_{ll}^{\delta+}$, indicating that some of the RD SW fibers shorten during full wetting (in a freely manner). The amplitude (A) and saturation half-times of the strain steps ($\tau_{1/2}$) of all tested SW fibers are obtained by curve fitting the strain data during the wetting period as displayed in Fig. 10. Figure 10 provides A and $\tau_{1/2}$ of each fiber separately (black open circles), together with the average values of the ensemble including the standard deviation of the mean (colored solid circles with error bars). Interestingly, for both A and $\tau_{1/2}$, the standard deviations of the mean do not overlap, indicating that the three fiber strain directions have a significantly different A and $\tau_{1/2}$. The fibers exhibit a more instantaneous step (lower $\tau_{1/2}$) in $\epsilon_{ll}^{\delta+}$, followed by a gradual increase (higher $\tau_{1/2}$) of $\epsilon_{tt}^{\delta+}$ over time, which is reflected at the sheet scale by a jump and subsequent gradual saturation of the *hydro*-expansion $\epsilon_{s}^{\delta+}$ (Fig. 6). In order to unravel this strain step, which is present in both the transient fiber and sheet *hydro*-expansion, a mechanism-based hypothesis is formulated next.

Hypothesis to explain the transient fiber and sheet hydro-expansion

To summarize the key observations so far, $\epsilon_{s}^{\delta+}$ and $MC_{s}^{\delta+}$ during the sheet-scale *hydro*-expansion response displayed a sudden step, which was also visible for the fiber-scale *hydro*-expansion. The step during the sheet-scale *hydro*-expansion was significantly larger for FD compared to RD. Similarly, the SW fibers exhibited an average step in $\epsilon_{ll}^{\delta+}$ which was larger for FD than RD. Finally, the SW fibers exhibit distinctly different longitudinal, transverse, and shear strain step magnitudes and saturation half-times during the wetting period.

In order to explain these observations, a comprehensive hypothesis is formulated which is speculative but consistent. Since both the handsheets and SW fibers display a strain step, the driving mechanism must probably reside within the fibers rather than, e.g., the inter-fiber bonds. As generally known, the fiber cell wall consists of stiff cellulose micro-fibrils, consisting of alternating crystalline and so-called "dislocated regions" (both constituting ~50% of the full micro-fibril), embedded inside an amorphous hemi-cellulose matrix (Agarwal et al. 2013). The hypothesized swelling mechanisms of a paper fiber (Fig. 5)

from dry (as-produced) to 90% RH is schematically depicted for FD and RD in Fig. 11, with the as-produced FD and RD fiber wall structure shown in (a) and the response after *hygro-* and *hydro*-expansion shown in, respectively, (b) and (c). Note that lignin is not drawn here, because the lignin content is below 0.3% ($\kappa < 2$), which is negligible to the cellulose and hemi-cellulose content, and lignin is much more hydrophobic. Hence, it is unlikely that lignin has a prominent effect.

Starting with the *hygro*-expansion, during water uptake, the hemi-cellulose (with a high porosity) absorbs most of the water and softens around 60% RH, whereas the "dislocated cellulose regions" inside the micro-fibrils (having a low porosity) only slightly swell, see (Salmén et al. 1987; Paajanen et al. 2022). Because the micro-fibril angle (MFA) of SW fibers is relatively low (Barnett and Bonham 2004; Cown et al. 2004), swelling of the hemi-cellulose results in relatively large transverse displacements and minor sliding of the micro-fibrils, yielding the $\bar{\epsilon}^{\gamma+}_{\underset{\Delta}{tt}}$ and $\bar{\epsilon}^{\gamma+}_{\underset{\Delta}{lt}}$ values of the fibers, whereas swelling of the "dislocated cellulose regions" is the main cause for the increase of $\bar{\epsilon}^{\gamma+}_{\underset{\Delta}{ll}}$ of the fibers (Fig. 5a). Please note that Fig. 5 displays the fiber strain changes during drying of RH cycles 1–2, which are similar to wetting (excluding the wetting slope of cycle 1), as, shown in Fig. 4. Furthermore, the swelling of the "dislocated cellulose" is larger for FD than RD (i.e. $\frac{L_1^{FD} - L_0^{FD}}{L_0^{FD}} > \frac{L_1^{RD} - L_0^{RD}}{L_0^{RD}}$), due to the alignment of the regions as a result of restrained drying as discussed in the introduction, hence the lower $\bar{\epsilon}^{\gamma-}_{\underset{\Delta}{ll}}$ in Fig. 5a. Because larger *MC* levels are attained during the fiber and handsheet *hydro*-expansion experiments compared to the 90% RH *hygro*-expansion measurements, this hypothesized swelling mechanism is extended to describe the step in strain and *MC* observed during the *hydro*-expansion of FD and RD, HW and SW handsheets and fibers (Figs. 6 and 9).

First, a hypothesis is proposed to explain the strain evolution of the handsheets and SW fibers during *hydro*-expansion, for the moment disregarding the type of drying procedure (FD or RD). For the handsheets, the step in $\epsilon_s^{\delta+}$ and $MC_s^{\delta+}$ occurs after the $MC_s^{\delta+}$ reaches a specific critical value (of around 20%), suggesting that the material exhibits a phase transformation, e.g. from (semi-)crystalline to amorphous. Note that this *MC* level is far above the 90% RH *MC* level. The already amorphous hemi-cellulose is unlikely to transform due to the higher *MC* level, whereas the crystalline cellulose regions remain stable, even at higher *MC* levels. Hence, the so-called "dislocated regions" in the cellulose micro-fibrils are expected to soften through a phase transformation (Marchessault and Howsmon 1957; Salmén 1982; Salmén et al. 1987; Agarwal et al. 2018). It is presumed that at a certain *MC* level, a critical capillary pressure is reached inside the fiber that is sufficiently high to "force" water molecules into the weak secondary bonds (hydrogen bonds) which are holding together the polymer chains in the "dislocated cellulose regions", thereby unlocking the inter-molecular bonds. This in turn results in softening of the "dislocated cellulose regions", entailing a sudden increase in water uptake in the now sparser molecular network. The timescales of unblocking the hydrogen bonds inside the "dislocated cellulose regions" (Fig. 10) are comparable to the timescales found for the transition of crystalline PEG networks (bonded by hydrogen bonds) to amorphous (breakage

of the hydrogen bonds) obtained during transient wetting and *hygro*-expansion of chain-extended ureido-pyrimidinone poly(ethylene glycol) (CE-UPy-PEG) hydrogel fibers Vonk et al. (2023b). This indicates that moisture-driven hydrogen bond breakage, driven by an abundant introduction of water, likely is the prominent driving mechanism here.

Considering the SW fibers, due to their low MFA, the process of softening of the "dislocated regions" in the cellulose micro-fibrils would mainly affect $\epsilon_{ll}^{\delta+}$, and to a lesser extent $\epsilon_{tt}^{\delta+}$ and $\epsilon_{lt}^{\delta+}$. In contrast, however, both $\epsilon_{tt}^{\delta+}$ and $\epsilon_{lt}^{\delta+}$ show steps that are significantly larger in magnitude and saturate slower than the step in $\epsilon_{ll}^{\delta+}$, as displayed in Fig. 10. This indicates the presence of a second mechanism that becomes active when the "dislocated cellulose regions" soften. To find an explanation for the different characteristics of the $\epsilon_{ll}^{\delta+}$, $\epsilon_{tt}^{\delta+}$, and $\epsilon_{lt}^{\delta+}$ curves, please consider that $\epsilon_{tt}^{\delta+}$ and $\epsilon_{lt}^{\delta+}$ are mainly driven by hemi-cellulose swelling and water residing between the micro-fibrils (pores), whereas $\epsilon_{ll}^{\delta+}$ is driven by swelling of the "dislocated cellulose regions" (Paajanen et al. 2022). Until the "dislocated cellulose regions" soften

Fig. 12 Comparison between the sheet-scale shrinkage during *hygro*-expansion ($\epsilon_{\Delta s}^{\gamma-}$) predicted by the analytical model, using the fiber shrinkage characteristics during *hygro*-expansion, i.e. $\bar{\epsilon}_{\Delta ll}^{\gamma-}$ and $\bar{\epsilon}_{\Delta tt}^{\gamma-}$ given in Fig. 5, and the experimental sheet-scale shrinkage ($\bar{\epsilon}_{\Delta s}^{\gamma-}$ given in Fig. 5a). The effect of the fibers' longitudinal to transverse stiffness ratio (E_l/E_t) and the free fiber length (η) is studied
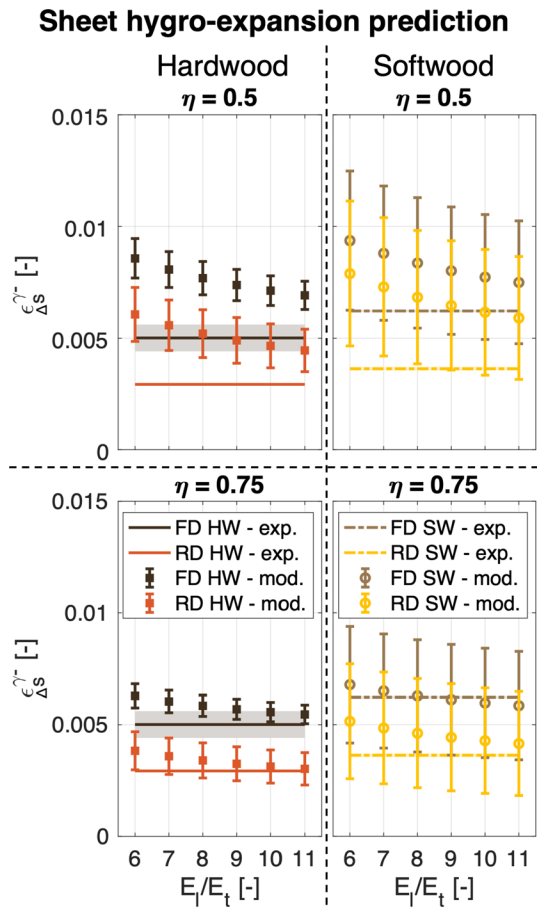
(leading to a jump in $\epsilon_{ll}^{\delta+}$, which is a fast process with a small $\tau_{1/2}$ of $\epsilon_{ll}^{\delta+}$ in Fig. 10), the hemi-cellulose ($\epsilon_{tt}^{\delta+}$ and $\epsilon_{lt}^{\delta+}$) was likely prevented from further swelling to its equilibrium volume, thus building up internal stress (pressure), which after softening of the "dislocated cellulose regions" starts to relax (gradually) through the uptake of more water (explaining the higher $\tau_{1/2}$). Hence, the hemi-cellulose was restrained from further swelling until unlocking and softening of the "dislocated cellulose regions". Probably candidates for this locking mechanism are (i) the helical micro-fibril structure in the fiber wall, as this requires the micro-fibrils to extend to enable the fiber to widen and/or lengthen; (ii) the interactions between the different S layers constituting the fiber wall, as kinematic compatibility of the S layers during swelling without building up residual stress is only feasible when the extension in the micro-fibril direction is not blocked. Furthermore, the smaller half-time of $\epsilon_{lt}^{\delta+}$ compared to $\epsilon_{tt}^{\delta+}$ in Fig. 10 may indicate that the sliding of the parallel micro-fibrils saturates faster after softening of the "dislocated cellulose regions" has completed, compared to the relative (perpendicular) movement of the fibrils accommodating $\epsilon_{tt}^{\delta+}$, which would be logical because softening of the "dislocated cellulose" mainly affects the longitudinal (parallel) micro-fibril direction.

Next, the effect of the drying procedure is incorporated into the hypothesis to explain the larger step in the transient $\epsilon_s^{\delta+}$ and $MC_s^{\delta+}$ during wetting of FD compared to RD handsheets, which also occurs later for FD than RD. Due to the alignment and stretching of, respectively, the cellulose micro-fibrils and the "dislocated cellulose regions" inside the micro-fibrils as a result of restrained drying, as represented in Fig. 11a, the "dislocated cellulose regions" in the RD fibers can stretch less (i.e. $\frac{L_2^{FD}-L_0^{FD}}{L_0^{FD}} > \frac{L_2^{RD}-L_0^{RD}}{L_0^{RD}}$) or they can even shrink when softening sets in, see Fig. 8b (Salmén et al. 1987; Khodayari et al. 2020). This explains the smaller step in the transient $\epsilon_s^{\delta+}$ for RD compared to FD handsheets, which is supported by the smaller average step in transient $\epsilon_{ll}^{\delta+}$ of the RD fibers compared to the FD SW fibers. Finally, after sufficiently long wetting under free boundary conditions, both the FD and RD fibers should "transform" to the same cell wall structure, which is shown in Fig. 11c with the same expected length of the (saturated) "dislocated cellulose regions" (i.e. $L_2^{FD} = L_2^{RD}$). In practice, however, as shown in Vonk et al. (2023c), RD SW fibers are not able to completely transform into FD fibers even after maintaining the SW fibers for 2 days in water, which was attributed to the fact that SW fibers typically have a partially collapsed lumen (due to their large diameter and small cell wall thickness), which prohibits rearrangement of the helical fiber structure. Even with this additional complexity, it can be concluded that all SW fiber and sheet-scale observations can be reasonably well explained with the proposed hypothesis of the softening of the "dislocated cellulose regions" unlocking further hemi-cellulose swelling. Moreover, the proposed hypothesis should equally hold for HW fibers. It is, however, less fruitful to apply this theory on the HW results, because the transient *hydro*-expansion response of the HW fibers is dictated by the slow introduction of water in the HW fiber experiments (see Fig. 2), which explains why no step in the strain components (with different timescales) is observed for the HW fibers.

Nevertheless, the hypothesis still explains the qualitative curves observed in the HW fibers.

Sheet-scale shrinkage predicted by the inter-fiber bond model

The sheet-scale shrinkage during *hygro*-expansion ($\underset{\Delta}{\epsilon}{}_s^{\gamma-}$) predicted by the inter-fiber bond model, using the fiber shrinkage characteristics during *hygro*-expansion, i.e. $\underset{\Delta}{\bar\epsilon}{}_{ll}^{\gamma-}$ and $\underset{\Delta}{\bar\epsilon}{}_{tt}^{\gamma-}$ displayed in Fig. 5, versus the transverse to longitudinal fiber stiffness ratio (E_t/E_l) for FD and RD, HW and SW is given in Fig. 12. The horizontal bands represent the experimentally obtained handsheet shrinkage ($\underset{\Delta}{\bar\epsilon}{}_s^{\gamma-}$) given in Fig. 5a including standard deviations.

Let us first only consider the results predicted by the model with a free fiber length (η) of the 0.5. The predicted sheet strain reduces when the longitudinal to transverse stiffness ratio (E_l/E_t) increases, which makes sense because the $\epsilon_{tt}^{\gamma-}$ contribution in the bonded area becomes less due to the relatively larger E_l of the bonded fiber. The model also correctly predicts that $\underset{\Delta}{\epsilon}{}_s^{\gamma-}$ of the FD sheets is larger than the RD sheets, and the SW larger than the HW, similar to the experiments. FD being larger than RD is mainly driven by the larger $\epsilon_{ll}^{\gamma-}$ being larger for FD, because $\epsilon_{tt}^{\gamma-}$ is almost equal for FD and RD. So the model predicts the correct trends. Quantitatively, however, the model clearly overpredicts $\underset{\Delta}{\epsilon}{}_s^{\gamma-}$, with the prediction only coming close to the experimentally obtained $\underset{\Delta}{\epsilon}{}_s^{\gamma-}$ for larger fiber stiffness ratios and only for SW.

One may argue, however, that the fiber bonds are actually only bonded for ~50%, e.g. Sormunen et al. (2019) showed using X-ray computed tomography with a high spatial resolution of 128 nm that the bonded area of various inter-fiber bonds (custom made with high pressures) is in reality around 60%. Earlier X-ray CT measurements (Wernersson et al. 2014; Borodulina et al. 2016; Urstöger et al. 2020) were performed with a spatial resolution of only ~0.5-1 μm, therefore, the measured bonded area may have been over-predicted. The effect of ~50% bonding of the inter-fiber bonds may be approximated by assuming that the free fiber length is around 75% (i.e. η equals 0.75), resulting in a significantly better match with the experiments, see Fig. 12. Additionally, η equals 0.75 is confirmed by Torgnysdotter et al. (2007) who found a fiber contact area of ~30% for non-surface-charged paper. Note that the transverse strain transfer is equal for bonds which are fully bonded or only bonded at the edges, because the transverse strain transfer is mostly carried out by the outer edges of the bonded area. hence, in reality, a larger *eta* can still result in the same sheet expansion as a lower η, which is not incorporated in the model. Furthermore, due to the considered orthogonal bond, the here-proposed model always predicts an overestimate of the actual sheet-scale shrinkage, as an additional diagonal fiber over the bonded area (as used in Bosco et al. (2015b)) would not change η, while it lowers $\epsilon_b^{\gamma-}$.

The model has also been assessed for predicting the sheet-scale *hydro*-expansion ($\underset{\Delta}{\epsilon}{}_s^{\delta}$) during wetting and drying using the fiber characteristics given in Fig. 8. However, for both the 50 and 75% free fiber length, the model significantly underpredicts the experimentally obtained $\underset{\Delta}{\epsilon}{}_s^{\delta}$ given in Table 4. This holds especially for

the FD sheets, which reveal a much larger experimental $\epsilon_{\Delta s}^{\delta}$ compared to the longitudinal fiber *hydro*-expansion. Possible explanations for this discrepancy may be the increased transverse strain contribution to the sheet scale during *hydro*-expansion. Furthermore, inter-fiber bonds may partially debond and rebond during the *hydro*-expansion experiments, hence changing the 3D geometry of network, whereas this is unlikely to occur in the *hygro*-expansion experiments. Finally, non-linear behavior such as plasticity is likely to occur at such high *MC* levels. Clearly, these effects are not incorporated into the simple model.

Even though the model is unable to predict the sheet-scale *hydro*-expansion of paper sheets, the model adequately matches the experiments for *hygro*-expansion, at least qualitatively. This demonstrates that such a (simple) analytical model is useful for identifying the ingredients governing the *hygro*-expansion behavior.

Conclusion

The *hygro*- and *hydro*-expansion of freely and restrained dried handsheets and fibers extracted from these handsheets have been investigated, allowing to explore the relevant mechanisms over time along with the accompanying dimensional changes. Previous works have suggested that the dimensional stability of a paper sheet is strongly affected by the stress applied during drying from a saturated state (due to liquid water, i.e. *hydro*-expansion) to lower moisture content (*MC*) levels, i.e. at 90% relative humidity (RH) (*hygro*-expansion). Therefore *hygro*-expansion measurements were conducted by changing the RH around fibers and handsheets, while *hydro*-expansion is realized by cooling the specimen to trigger condensation at the fibers and handsheets. To monitor the sheet *hydro*-expansion, a novel method was developed. During all experiments, the dimensional changes are determined using state-of-the-art digital image correlation techniques, enabling the continuous transient full-field (longitudinal, transverse and shear) fiber, and (isotropic) in-plane sheet *hygro*- and *hydro*-expansion. Additionally, the transient *MC* has also been monitored during the sheet *hydro*-expansion measurements. Furthermore, the experimental fiber and sheet data enables to assess a simple inter-fiber bond model in order to predict the sheet expansion from the experimentally obtained fiber characteristics for various ratios between the longitudinal and transverse fiber stiffness.

For *hygro*- and *hydro*-expansion, the freely dried handsheets shrink more than the restrained dried, and the softwood handsheets shrink more than the hardwood. Furthermore, the longitudinal fiber *hygro*- and *hydro*-expansion is distinctly lower for restrained drying, explaining the sheet-scale differences, because it was found that the transverse strain contribution to the sheet scale is relatively low. The transient sheet-scale *hydro*-expansion experiments reveal a sudden step in strain and *MC*, which was also visible in the transient *hydro*-expansion of freely dried softwood fibers. This step was attributed to the capillary pressure inside the fiber reaching a critical level, "forcing" the water into the so-called "dislocated cellulose regions" inside the micro-fibrils, which consequently soften, enabling the fiber to continue swelling. During the handsheet *hydro*-expansion experiments,

the strain step is significantly larger and occurs at higher *MC* levels for freely dried compared to restrained dried handsheets. The difference in magnitude of the strain step is attributed to the "dislocated regions" in the cellulose micro-fibrils being stretched as a result of restrained drying, therefore not being able to stretch upon softening, in contrast to their freely dried counterparts. This hypothesis is strongly supported by the restrained dried softwood fibers which reveal both swelling and shrinkage in longitudinal direction when the softening is expected to occur, whereas the freely dried fibers only show swelling, explaining the lower resulting strain step for the restrained dried handsheets. Considering that most of the deformation due to a change in moisture content occurs within seconds/ minutes, the phenomena observed during the fiber- and sheet *hygro-* and *hydro-* expansion experiments presented here likely also occur during fast processes such as inkjet printing.

The inter-fiber bond model qualitatively predicts the sheet *hygro-*expansion trends, i.e. the larger *hygro-*expansion of (i) FD compared to RD handsheets, and (ii) SW compared to HW handsheets. A decreasing trend in sheet expansion for an increasing longitudinal to transverse fiber stiffness ratio is predicted by the inter-fiber bond model. Furthermore, the model overestimates the sheet-scale *hygro-*expansion for a free fiber length of 0.5. A free fiber length of 0.75 was also assessed, which complies better with the literature, resulting in a better quantitative match between the model and the experiments for *hygro-*expansion. Regarding *hydro-*expansion, the model underpredicts the experiments, which could be due to the simplicity of the model missing some key features affecting *hydro-*expansion.

Author Contributions NV: Conceptualization, Methodology, Software, Validation, Investigation, Writing - original draft, Visualization. WS: Conceptualization, Methodology, Investigation. TA: Methodology, Investigation. RP: Methodology, Supervision, Funding acquisition. MG: Resources, Writing - review & editing, Supervision, Funding acquisition. JH: Conceptualization, Methodology, Validation, Resources, Writing - review & editing, Supervision, Funding acquisition.

Data availability The presented data will be made available on request.

Declarations

Conflict of interest The authors declare that they have no known competing financial interests or personal relationships that could have appeared to influence the work reported in this work.

Ethical approval This article does not contain any studies with human participants or animals performed by any of the authors.

Consent for publication The authors hereby consent to publication of the present research work in this journal, if selected for publication.

References

Agarwal UP, Ralph SA, Reiner RS, Baez C (2018) New cellulose crystallinity estimation method that differentiates between organized and crystalline phases. Carbohyd Polym 190:262–270

Agarwal UP, Reiner RR, Ralph SA (2013) Estimation of cellulose crystallinity of lignocelluloses using near-IR FT-Raman spectroscopy and comparison of the Raman and Segal-WAXS methods. J Agric Food Chem 61:103–113

Alzweighi M, Mansour R, Lahti J, Hirn U, Kulachenko A (2021) The influence of structural variations on the constitutive response and strain variations in thin fibrous materials. Acta Mater 203:116460

Barnett JR, Bonham VA (2004) Cellulose microfibril angle in the cell wall of wood fibres. Biol Rev 79:461–472

Borodulina S, Kulachenko A, Wernersson ELG, Luengo Hendriks CL (2016) Extracting fiber and network connectivity data using microtomography images of paper. Nord Pulp Pap Res J 31:469–478

Bosco E, Bastawrous MV, Peerlings RHJ, Hoefnagels JPM, Geers MGD (2015) Bridging network properties to the effective hygro-expansivity of paper: experiments and modelling. Phil Mag 95:3385–3401

Bosco E, Peerlings RHJ, Geers MGD (2015) Predicting hygro-elastic properties of paper sheets based on an idealized model of the underlying fibrous network. Int J Solids Struct 56:43–52

Bosco E, Peerlings RHJ, Geers MGD (2017) Asymptotic homogenization of hygro-thermo-mechanical properties of fibrous networks. Int J Solids Struct 115:180–189

Bosco E, Peerlings RHJ, Geers MGD (2017) Hygro-mechanical properties of paper fibrous networks through asymptotic homogenization and comparison with idealized models. Mech Mater 108:11–20

Brandberg A, Motamedian HR, Kulachenko A, Hirn U (2020) The role of the fiber and the bond in the hygroexpansion and curl of thin freely dried paper sheets. Int J Solids Struct 193:302–313

Cown DJ, Ball RD, Riddell MJC (2004) Wood density and microfibril angle in 10 Pinus radiata clones: distribution and influence on product performance. NZ J Forest Sci 34:293

Czibula C, Brandberg A, Cordill MJ, Matković A, Glushko O, Czibula C, Kulachenko A, Teichert C, Hirn U (2021) The transverse and longitudinal elastic constants of pulp fibers in paper sheets. Sci Rep 11:1–13

Fellers C (2007) The interaction of paper with water vapour. Pap Prod Phys Technol. https://doi.org/10.1515/9783110213461.109

Jajcinovic M, Fischer WJ, Mautner A, Bauer W, Hirn U (2018) Influence of relative humidity on the strength of hardwood and softwood pulp fibres and fibre to fibre joints. Cellulose 25:2681–2690

Jentzen CA (1964) The effect of stress applied during drying on some of the properties of individual pulp fibers. In: Ph.D. thesis. Georgia Institute of Technology

Joffre T, Isaksson P, Dumont PJJ, Roscoat S, Sticko S, Orgéas L, Gamstedt EK (2016) A method to measure moisture induced swelling properties of a single wood cell. Exp Mech 56:723–733

Khodayari A, Van Vuure AW, Hirn U, Seveno D (2020) Tensile behaviour of dislocated/crystalline cellulose fibrils at the Nano scale. Carbohyd Polym 235:115946

Kulachenko A, Gradin P, Uesaka T (2005) Tension wrinkling and fluting in heatset web offset printing process. Post buckling analyses. In: 13th fundamental research symposium on advances in paper science and technology, Location: Univ Cambridge, Cambridge, ENGLAND Date: SEP, 2005, The Pulp and Paper Fundamental Research Society, pp 1075–1099

Larsson PA, Hoc M, Wågberg L (2009a) The influence of grammage, moisture content, fibre furnish and chemical modifications on the hygro-and hydro-expansion of paper. In: 14th fundamental research symposium on advances in pulp and paper research, Location: St Annes Coll, Oxford, ENGLAND Date: SEP 13-18, 2009, pp 355–388

Larsson PA, Hoc M, Wågberg L (2009) A novel approach to study the hydroexpansion mechanisms of paper using spray technique. Nord Pulp Pap Res J 24:371–380

Larsson PA, Wågberg L (2008) Influence of fibre-fibre joint properties on the dimensional stability of paper. Cellulose 15:515–525

Magnusson MS, Östlund S (2013) Numerical evaluation of interfibre joint strength measurements in terms of three-dimensional resultant forces and moments. Cellulose 20:1691–1710

Marchessault RH, Howsmon JA (1957) Experimental evaluation of the lateral-order distribution in cellulose. Text Res J 27:30–41

Meylan BA (1972) The influence of microfibril angle on the longitudinal shrinkage-moisture content relationship. Wood Sci Technol 6:293–301

Motamedian HR, Kulachenko A (2019) Simulating the hygroexpansion of paper using a 3D beam network model and concurrent multiscale approach. Int J Solids Struct 161:23–41

Nanko H, Wu J (1995) Mechanisms of paper shrinkage during drying. In: International paper physics conference. Niagara-on-the-Lake, Canada, pp 103–113

Neggers J, Blaysat B, Hoefnagels JPM, Geers MGD (2016) On image gradients in digital image correlation. Int J Numer Meth Eng 105:243–260

Niskanen KJ, Kuskowski SJ, Bronkhorst CA (1997) Dynamic hygroexpansion of paperboards. Nord Pulp Pap Res J 12:103–110

Paajanen A, Zitting A, Rautkari L, Ketoja JA, Penttilä PA (2022) Nanoscale mechanism of moisture-induced swelling in wood microfibril bundles. Nano Lett 22:5143–5150

Page DH, Tydeman PA (1963) Transverse swelling and shrinkage of softwood tracheids. Nature 199:471–472

Pister KS, Dong SB (1959) Elastic bending of layered plates. J Eng Mech Div 85:1–10

Reissner E, Yl Stavsky (1961) Bending and stretching of certain types of heterogeneous aeolotropic elastic plates. J Appl Mech 28:402–408

Salmén L, Fellers C, Htun M (1985) The in-plane and out-of-plane hygroexpansional properties of paper. Papermak Raw Mater 2:511–527

Salmén L (1982) Temperature and water induced softening behaviour of wood fiber based materials. In: Ph.D. thesis. Department of Paper Technology, Royal Institute of Technology Stockholm

Salmén L, Fellers C, Htun M (1987) The development and release of dried-in stresses in paper. Nord Pulp Pap Res J 2:44–48

Samantray P, Peerlings RHJ, Bosco E, Geers MGD, Massart TJ, Rokoš O (2020) Level set-based extended finite element modeling of the response of fibrous networks under hygroscopic swelling. J Appl Mech 87:101005

Shafqat S, Hoefnagels JPM (2021) Cool, dry, nano-scale DIC patterning of delicate, heterogeneous, non-planar specimens by micro-mist nebulization. Exp Mech 61:917–937

Sormunen T, Ketola A, Miettinen A, Parkkonen J, Retulainen E (2019) X-ray nanotomography of individual pulp fibre bonds reveals the effect of wall thickness on contact area. Sci Rep 9:1–7

Torgnysdotter A, Kulachenko A, Gradin P, Wågberg L (2007) The link between the fiber contact zone and the physical properties of paper: a way to control paper properties. J Compos Mater 41:1619–1633

Tydeman PA, Wembridge DR, Page DH (1966) Transverse shrinkage of individual fibres by micro-radiography. In: Consolidation of the paper web, pp 119–144

Uesaka T (1994) General formula for hygroexpansion of paper. J Mater Sci 29:2373–2377

Uesaka T, Moss C, Nanri Y (1992) The characterization of hygroexpansivity of paper. J Pulp Pap Sci 18:J11–J16

Urstöger G, Kulachenko A, Schennach R, Hirn U (2020) Microstructure and mechanical properties of free and restrained dried paper: a comprehensive investigation. Cellulose 27:8567–8583

Vonk N, van Weele S, Slokker G, van Maris M, Hoefnagels J (2023) Challenges and solutions of environmental scanning electron microscopy characterisation of biomaterials: application to hygro-expansion of paper. Strain 59(4):e12440

Vonk NH, van Adrichem SC, Wu DJ, Dankers PY, Hoefnagels JP (2023) Full-field hygroscopic characterization of tough 3D-printed supramolecular hydrogels. J Polym Sci 61(12):1120–1131

Vonk NH, Geers MGD, Hoefnagels JPM (2021) Full-field hygro-expansion characterization of single softwood and hardwood pulp fibers. Nord Pulp Pap Res J 36:61–74

Vonk NH, Peerlings RHJ, Geers MGD, Hoefnagels JPM (2023) Effect of restrained versus free drying on hygro-expansion of hardwood and softwood fibers and paper handsheet. Cellulose 30:11135–11156

Vonk NH, Peerlings RHJ, Geers MGD, Hoefnagels JPM (2023d) Re-understanding the in-plane hygro-expansion of freely and restrained dried paper handsheets. In: 17th Fundamental Research Society Symposium 2022. Pulp & Paper Fundamental Research Society (FRC), pp 421–440

Vonk NH, Peerlings RHJ, Geers MGD, Hoefnagels JPM (2024) Full-field hygroscopic characterization of paper inter-fiber bonds and the implications on network hygro-expansivity. Cellulose 31:567–586

Vonk NH, Verschuur NAM, Peerlings RHJ, Geers MGD, Hoefnagels JPM (2020) Robust and precise identification of the hygro-expansion of single fibers: a full-field fiber topography correlation approach. Cellulose 27:6777–6792

Weise U, Paulapuro H (1995) Changes of pulp fibre dimensions during drying. In: International paper physics conference, Niagara-on-the-Lake, 11.-14.9. 1995, Technical Section CPPA & TAPPI. pp 121–124

Wernersson ELG, Borgefors G, Borodulina S, Kulachenko A (2014) Characterisations of fibre networks in paper using micro computed tomography images. Nord Pulp Pap Res J 29:468–475